# On the evolution of Middle Triassic passive margins of the Greater Adria Plate : inferences from the study of calc-alkaline and shoshonitic tuffs from NW Croatia

**Slovenec, Damir; Horvat, Marija; Smirčić, Duje; Belak, Mirko; Badurina, Luka; Kukoč, Duje; Grgasović, Tonći; Byerly, Kevin; Vukovski, Matija; Šegvić, Branimir**

*Source / Izvornik:* **Ofioliti, 2023, 48, 31 - 46**

**Journal article, Published version**
**Rad u časopisu, Objavljena verzija rada (izdavačev PDF)**

*Permanent link / Trajna poveznica:* https://urn.nsk.hr/urn:nbn:hr:169:756842

# ON THE EVOLUTION OF MIDDLE TRIASSIC PASSIVE MARGINS OF THE GREATER ADRIA PLATE: INFERENCES FROM THE STUDY OF CALC-ALKALINE AND SHOSHONITIC TUFFS FROM NW CROATIA

**Damir Slovenec*, Marija Horvat*, Duje Smirčić**, Mirko Belak*, Luka Badurina***, Duje Kukoč*,✉, Tonći Grgasović*, Kevin Byerly***, Matija Vukovski*** and **Branimir Šegvić*****

* *Croatian Geological Survey, Zagreb, Croatia.*
** *Faculty of Mining, Geology and Petroleum Engineering, University of Zagreb, Croatia.*
*** *Department of Geosciences, Texas Tech University, Lubbock TX, U.S.A.*
✉ *Corresponding author, email: dkukoc@hgi-cgs.hr*

**Keywords:** *acidic pyroclastic rocks; Middle Triassic; Greater Adria Plate; Tethyan continental margin; NW Croatia.*

ABSTRACT

Rhyolitic tuffs are readily found within the Northwestern Croatian Triassic Rift Basin which akems the southernmost segment of the geotectonic unit of the Southern Alps. The latter, located in the SW segment of the Zagorje-Mid-Transdanubian shear Zone, provides insights into the volcanism and geodynamic history of the passive margins of the Greater Adria Plate during the Middle Triassic. The eruptions at the time produced material that was distributed through air-fall transport and pyroclastic density currents, and after deposition gave rise to acidic pyroclastic rocks of the Pietra Verde type. These rocks are homogeneous to horizontally laminated, showing intervals of normal gradation and appear as vitroclastic, vitrocrystalloclastic, and crystalloclastic tuffs. Late Anisian-early Ladinian sub-alkaline, middle to high-K calc-alkaline, and shoshonitic tuffs feature a LREE over HREE enrichment, high LILE content, and HFSE depletion. Negative anomalies of the Nb-Ta pair, P, Sr, Eu, and Ti coupled with variable positive and negative spikes of Pb and Ba, respectively were also documented. An important contribution of the continental material in the evolution of the studied acidic rocks is attested by negative values of initial $\varepsilon_{Nd}$ (-2.7 to -4.95). Tuff petrogenesis essentially included melting of the heterogeneous lithospheric (subcontinental) mantle, subordinated melting of the continental crust and fractional crystallization of feldspar. Studied tuffs originated in a continental margin volcanic arc(?) environment formed during an active(?) northward subduction of the Paleotethyan lithosphere beneath the Eurasian Plate or, alternatively, more likely, during the passive continental rifting along the margins of the Greater Adria Plate.

## INTRODUCTION

The origin of the Tethyan Mesozoic Adriatic-Dinaridic carbonate platforms, i.e., Southern Tethyan Megaplatform, associated with intense volcanic activity during the Middle Triassic, has been proposed by many authors (e.g., Pamić, 1984; Castellarin et al., 1988; Trubelja et al., 2004; Pamić and Balen, 2005; Goričan et al., 2005; Vlahović et al., 2005; Storck et al., 2018; Smirčić et al., 2018 and reference therein). These igneous events in the Adria Plate, i.e. Alpine-Carpathian Belt, including Southern Alps, Dinarides and Hellenides are characterized by multi-phase lava flow extrusions and deposition of different types of pyroclastic rocks (e.g., Bonadiman et al., 1994; Harangi et al., 1996; Trubelja et al., 2004; Saccani et al., 2015; Casetta et al., 2018; Storck et al., 2018; 2020; Lustrino et al., 2019; Maurer et al., 2019; De Min et al., 2020; Slovenec et al., 2020; Castorina et al., 2020; Slovenec and Šegvić, 2021). Nevertheless, the geodynamic framework and tectonomagmatic evolution of the aforementioned areas, including the Adria Plate, separating Gondwana and Laurasia is still controversial and a subject of debate (e.g., Stampfli and Borel, 2004; Stampfli et al., 2013; Zulauf et al., 2018; Neubauer et al., 2019; Van Hinsberger et al., 2020; De Min et al., 2020 and references therein). The geodynamic evolution of the transitional zone of the Southern Alps and the Dinarides assumes a collage of compressional, extensional, and/or transtensional movements (Tomljenović et al., 2008; Van Gelder et al., 2015). The complex geodynamic lithosphere processes along the continental margins of the Adria during the Triassic period, can therefore be unveiled solely by the systematic study of volcanic-sedimentary successions formed in such geodynamic environment (e.g., Castellarin et al., 1988; Bonadiman et al., 1994; Stampfli et al., 2002; Schmid et al., 2008; Storck et al., 2018; Maurer et al., 2019; Lustrino et al., 2019 and reference therein).

Middle Triassic volcanic-sedimentary successions of the southernmost segment of the geotectonic unit of the Southern Alps (*sensu* Schmid et al., 2008) crop out in the intra-Pannonian Mts. (Ivanščica, Strahinjščica, Kuna Gora, Desinić Gora, and Ravna Gora) of northwestern Croatia (Figs. 1a, b and 2) which are part of the southwestern portion of the Zagorje-Mid-Transdanubian shear Zone (ZM-TDZ, *sensu* Pamić and Tomljenović, 1998).

These successions, which form the Northwestern Croatian Triassic Rift Basin (NCTRB in Kukoč et al., 2023), are predominantly represented by pyroclastic acidic rocks intercalated with deep-sea siliceous and carbonate sediments (e.g., Šebečić, 1969; Šimunić and Šimunić, 1997; Šimunić et al., 1982). The acidic pyroclastic rocks of the southern slopes of the mountains of Kuna Gora, Strahinjščica, and Ivanščica (Figs. 2 and 3), are stratigraphically positioned as late Anisan to early Ladinian, based on the fossil content of radiolarians (Kukoč et al., 2023).

The goal of this paper is to provide a detailed account on pyroclastic rocks' mineralogy, geochemistry, petrology, and isotopic composition to draw inferences on petrogenesis and geotectonic environment these rocks formed in during the late Anisian to early Ladinian. This approach will contribute to the understanding of the geodynamic events having taken place along the passive margin of the Greater Adria Plate and Tethys during the Middle Triassic.

## GEOLOGICAL SETTING

The studied acidic pyroclastic rocks make an integral part of the Middle Triassic volcanic-sedimentary succession of the Northwestern Croatian Triassic Rift Basin, which commonly crops out along the southern slopes of the mountains Kuna Gora, Strahinjščica and Ivanščica (Figs. 2 and 3) located at the SW tip of the Zagorje-Mid-Transdanubian shear Zone (Fig. 1b). This geotectonic unit, derived from the continental crustal domains, is pressed between the two regional fault systems, namely the Zagreb-Zemplín Line to the south and the Periadriatic-Balaton Line to the north (e.g., Harangi et al., 1996; Haas and Kovács, 2001). A series of north-Croatian mountains (Fig. 1b) defines a transitional realm between two regional geotectonic units: the Southern Alps and the Dinarides (Fig. 1a). Moreover, the area is marked by the present-day NNW-verging Dinaridic structures which are overprinted by S-verging Alpine structures (e.g., Van Gelder et al., 2015).

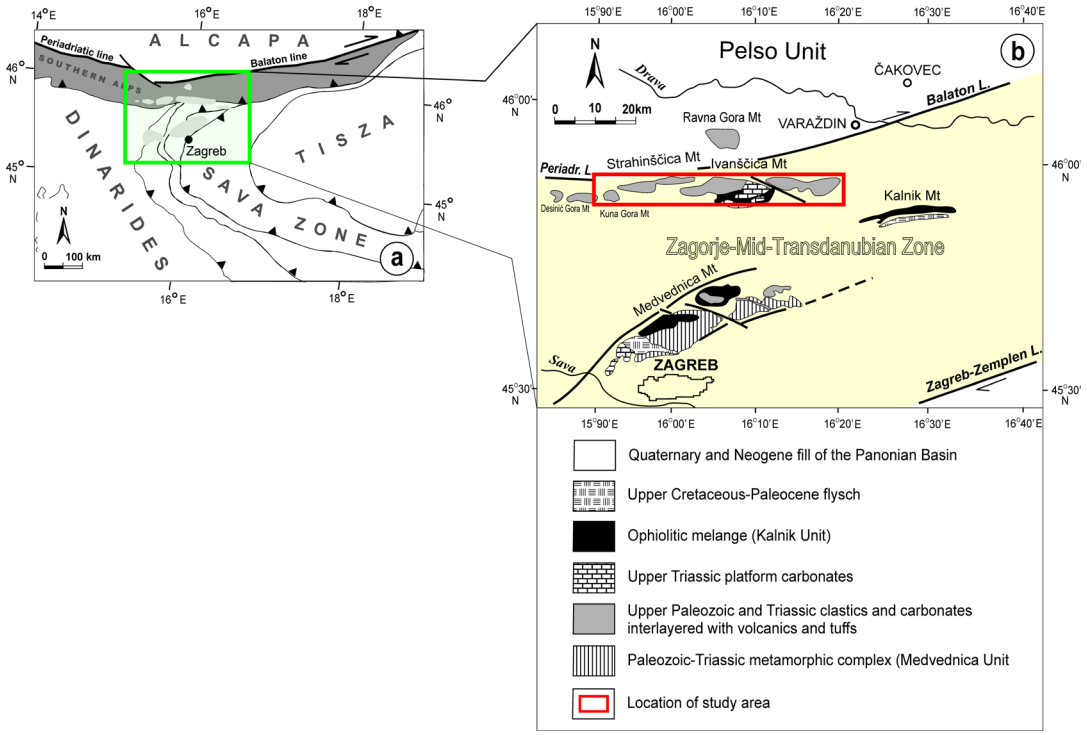


Fig. 1 - a) Geotectonic sketch map of the major tectonic units (simplified after Schmid et al., 2008). b) Geological sketch map of the Croatian part of the Zagorje-Mid-Trandanubian Zone (slightly modified after Pamić and Tomljenović, 1998).

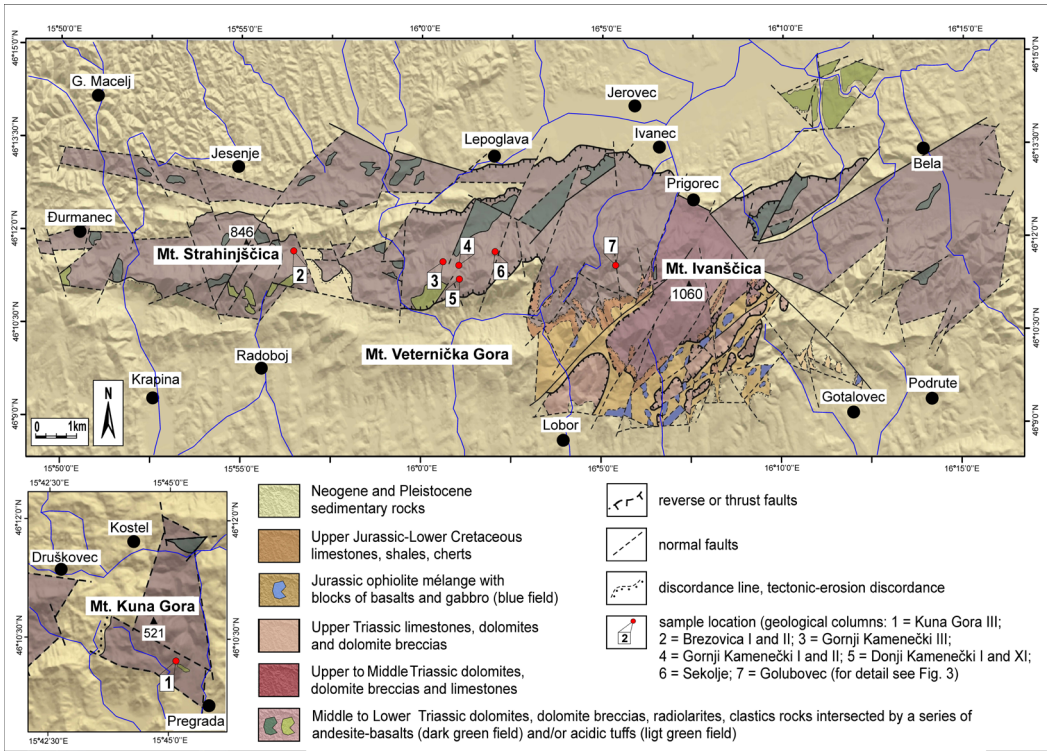


Fig. 2 - Simplified geological sketch map of the Kuna Gora, Strahinjščica and Ivanščica Mts. (modified after Šimunić et al., 1982). The reader is referred to the PDF version of the article for a colour version.

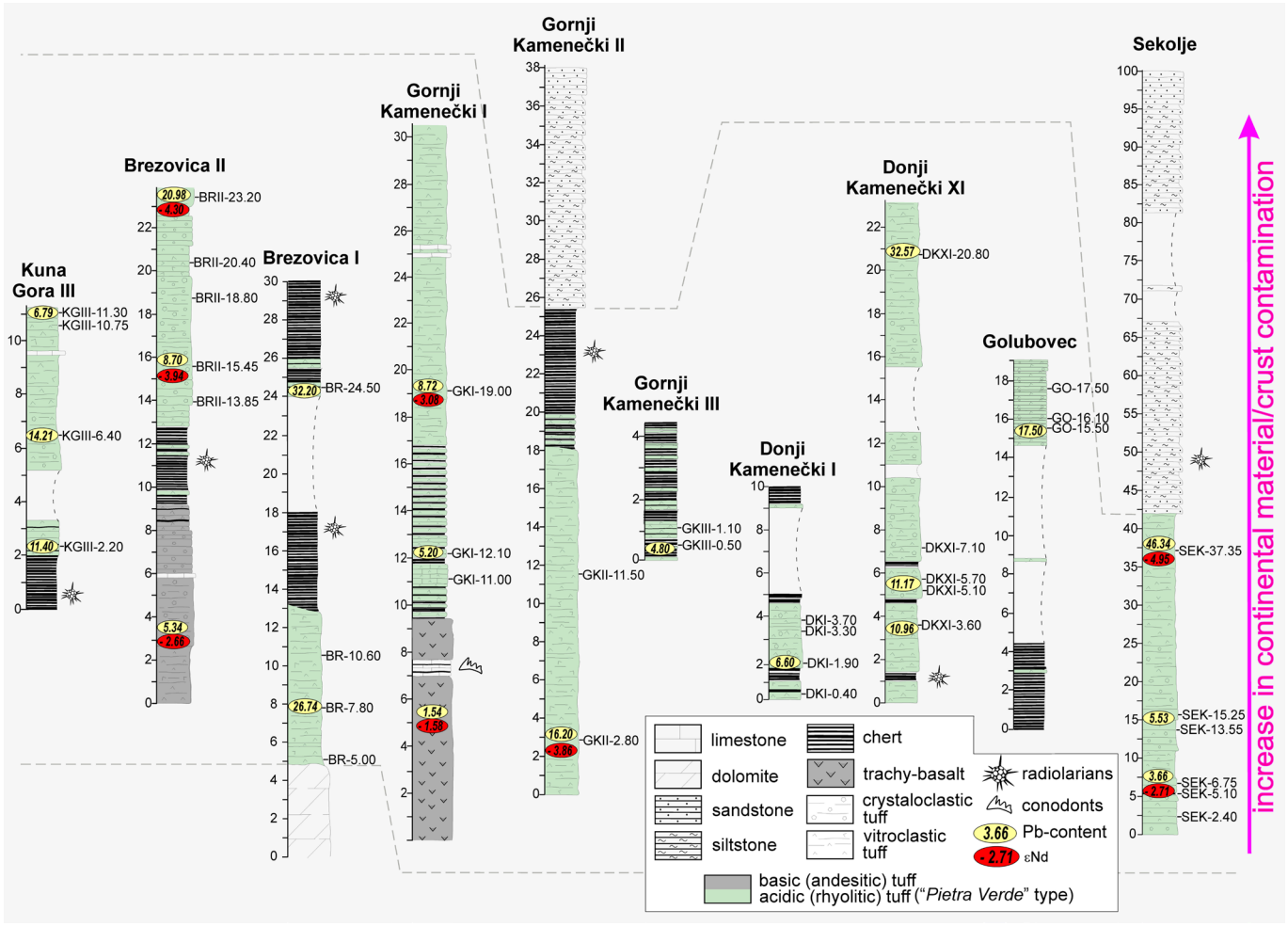


Fig. 3 - The position of analyzed samples on lithological columns of investigated area (modified after Kukoč et al., in review).

The geological structure of the mountains Kuna Gora, Strahinjščica and Ivanščica is relatively simple and includes Triassic shallow to deep-sea volcanic-sedimentary successions of the passive continental margin of Adria (Fig. 2) which belong to the southernmost segment of the geotectonic unit of Southern Alps (*sensu* Schmid et al., 2008; Fig. 1a). Triassic carbonate and clastic strata are unconformably overlain by Tertiary and Quaternary deposits or appear to be in a tectonic contact (Fig. 2). Volcanic and pyroclastic rocks of the area, presented by the basic and intermediate to acidic lithologies, are intercalated with mid-Triassic siliciclastics, radiolarites and carbonates (e.g., Marci et al., 1982; 1984; Goričan et al., 2005; Slovenec et al., 2020; Slovenec and Šegvić, 2021; Kukoč et al., in review). Volcanic rocks which crop out at the northern slopes of Kuna Gora and Strahinjščica Mts. and the northern part of Ivanščica Mt. are characterized by calc-alkaline andesitic to basaltic lava flows. These Anisian to Ladinian lithologies are thought to indicate rift-related magmatism (Slovenec et al., 2020; Slovenec and Šegvić, 2021- see Fig. 14). The formation of this magmas is linked to the subduction of the older Paleotethys lithosphere either beneath the European Plate (Stampfli and Borel, 2004) or the Greater Adria Plate (Van Hinsbergen et al., 2020). On the other hand, the southern slopes of Kuna Gora, Strahinjščica and Ivanščica Mts. host peculiar occurrences of *Pietra Verde* tuff intercalated in deep-marine sedimentary successions (Figs. 2 and 3), which is studied in detail in this paper.

## MATERIALS AND METHODS

Fifty-two representative rock samples from 10 geological sections (Fig. 2) were selected for further investigation. The rocks' petrographic characteristics were studied using an Optika B-1000 POL polarizing microscope equipped with a CP6-FL camera installed at University of Zagreb's Faculty of Mining, Geology and Petroleum Engineering. The pyroclastic deposits were classified according to the scheme proposed by Cook (1965) and Schmid (1981).

The mineral compositions of three representative samples were analyzed at the University of Geneva's Department of Earth Sciences using a JEOL JXA 8200 Superprobe equipped with five wavelength dispersive spectrometers. Operating parameters included an accelerating voltage of 20 kV, a 15 nA beam current, and a defocused beam of ~ 10 $\mu$m. Counting times of 30 s on peak and 15 s on background on both sides of the peak were used for all elements, except for Na and K, which were measured 20 s and 10 s on peak and background, respectively, due to their high mobility under an electron beam. For this reason, Na and K were also measured first. Limits of detection (LOD) were calculated as the minimum concentration required to produce count rates three times higher than the square root of the background (3σ; 99 wt% degree of confidence at the lowest detection limit). Concentrations below the LOD are reported as not detected. Raw data were corrected for matrix effects using

the ϕϱZ method by Armstrong (1991). Natural minerals, oxides (corundum, spinel, hematite, and rutile), and silicates (albite, orthoclase, anorthite, and wollastonite) were used for calibration. Mineral formulas were calculated using a software package MINPET written by Linda R. Richard (Gatineau, Québec, Canada).

The least altered representative samples were selected for the bulk-rock chemical analyses. Bulk-rock powders for chemical analyses of 19 samples were analyzed by XRF for major elements, and ICP-MS for trace elements at Texas Tech University's Department of Geosciences and Actlab Laboratories. Assessment of accuracy and precision for trace elements measured at Texas Tech University was measured using the USGS BHVO-2 analytical glass standards (Johum, 2005; Supplementary Material Tables S1-S2-S3; for details see Segvić et al., 2022). At Actlab Laboratories major and trace elements concentrations were measured using USGS BHVO-2, W-2 and BIR-1 reference materials with accuracy and precision better than ±1% and ±5%, respectively. It is 3σ at 10 times detection limit. Detection limit: $TiO_2$, MnO - 0.001 wt%; $SiO_2$, $Al_2O_3$, $Fe_2O_3$, MgO, CaO, $Na_2O$, $K_2O$, $P_2O_5$ = 0.01 wt%; Lu = 0.002 ppm; Eu = 0.005 ppm; Ta, Pr, Sm, Gd, Ho, Er, Yb, U = 0.01 ppm; Th, La, Ce, Nd, Tm = 0.05 ppm; Cs, Hf = 0.1 ppm; Nb = 0.2 ppm; Y = 0.5 ppm; Sc, Rb, Zr = 1 ppm; Sr = 2 ppm; Ba = 3 ppm; V, Pb = 5 ppm; Cr, Ni = 20 ppm. The quality of the measurements was checked by replicating the analysis on ~ 12% of the samples.

Nd isotopic compositions of six bulk rock samples were measured at the Noble Gas Laboratory Pacific Centre for Isotopic and Geochemical Research, University of British Columbia using a Triton Plus mass spectrometer. Normalizing ratios of $^{146}Nd/^{144}Nd = 0.7219$ were assumed. The average JNd-i standard run at $^{143}Nd/^{144}Nd = 0.512079 \pm 0.000008$ (n = 9.2 standard deviations). The data is reported relative the recommended value of $^{143}Nd/^{144}Nd = 0.5$ $^{143}Nd/^{144}Nd = 0.512637 \pm 0.000012$ (Weis et al., 2006). Total procedural blanks were less than 10pg.

X-ray Powder Diffraction (XRD) was performed on the global particle fraction on a set of 21 samples. Sample preparation included initial material powdering in an agate mortar prior to whole rock measurements. The measurements were undertaken at the Geosciences Clay Laboratory of Texas Tech University using a Bruker D8 Advance diffractometer. This instrument features a horizontal goniometer axis and synchronized rotation of both the X-ray source and detector arms. Measurements consisted of a step scan in the Bragg-Brentano geometry with CuK$\alpha$ radiation (40 kV and 40 mA). Sample mounts were scanned for 1.8 s per 0.02°, from 3° to 70° 2$\theta$. XRD traces interpretation was accomplished using Bruker EVA software and comparison against the PDF4 database issued by the International Centre for Diffraction Data.

## RESULTS

### Petrography and mineral chemistry of *Pietra Verde* tuffs

The *Pietra Verde* pyroclastic facies (Du Riche Preller, 1916) was documented in all the sections presented in this study (Fig. 3). The three different lithotypes were distinguished: vitroclastic (VC), vitrocrystalloclastic (VCC), and crystalloclastic (CC) tuffs (Fig. 4). The tuffs are homogeneous (Fig. 4a) to horizontally laminated (Fig. 4b) and normally graded.

*Vitroclastic tuffs* are composed of fine to medium ash glass shards and pumice fragments. The fine ash component is dominant in this lithotype. Due to their size, the shape of shards is not clearly distinguishable (Fig. 4a). The medium sized shards have visible forms, varying from arcuate, platy, *x*- to *y*-shaped, to rare bubble wall (Fig. 4c). Glass shards occupy from 70 to 100 vol% of the rock. In addition to glass shards, pumice fragments, and crystalloclasts are also present. The content of pumice fragments varies from 5 to 20 vol% (Fig. 4d). The size of pumice fragments is commonly a medium ash size (~ 0.5 mm). All pumice fragments are altered to sheet silicates (Fig. 4e, Table 2), with rare vesicles filled by microcrystalline quartz. In some samples, pumice fragments are oriented showing imbrication patterns. Crystalloclasts occupy up to 10 vol% of the rocks. The crystalloclastic particles are presented by mostly feldspar (5 to 7 vol%) and quartz (3 to 5 vol%). Feldspar is partially altered to clay minerals and calcite. The exception is the prismoidal, euhedral to subhedral feldspar from section DK I (Fig. 4f). Quartz crystalloclasts appear in irregularly shaped grains. The matrix of this lithotype is composed of fine volcanic ash particles, not determinable by micropetrographical analysis. Chloritization, celadonitization, calcitization and silicification of the fine matrix is noticied. This lithotype occurs in all the investigated sections and renders the most dominant lithotype of Middle Triassic pyroclastic deposits of NW Croatia (Fig. 3).

*Vitrocrystalloclastic tuffs* are composed of vitric and crystalloclastic particles with ratios ranging from 80/20 to 50/50. With respect to vitric components' shapes, size and alteration processes, no difference has been reported across the tuffs' lithotype except the existence of larger (around 1 mm) pumice fragments (Fig. 4g) in the case of vitrocrystalloclastic tuffs. Particles are largely of medium ash size, while some pumice fragments and crystalloclasts exceed the lapilli sized particles. The most abundant crystalloclasts is plagioclase (0.7 to 2.5 mm), followed by K-feldspar and quartz, and sporadically a pleochroic micaceous phase. The exception is the sample SEK-15.25 dominated by crystalloclasts of quartz. Subhedral to euhedral crystalloclasts of plagioclase are commonly fragmented and occasionally exhibit a jig-saw fit texture (Fig. 4h). Plagioclase is moderately altered to sericite, prehnite, and clay minerals. Alkali feldspar is mostly of euhedral shape or subordinately altered to clay mineral aggregates. The chemical composition (Table 1) of K-feldspar is uniform ($An_{0.3\text{-}0.4}Ab_{4.6\text{-}5.3}Or_{94.1\text{-}95.0}$), while that of plagioclase is weakly variable and corresponds to albite and peristerite ($An_{2.4\text{-}9.2}Ab_{90.3\text{-}91.2}Or_{05.1\text{-}6.7}$; Fig. 5). The shape of quartz crystalloclasts (up to 1 mm) vary from angular to rounded with remarkable oval cavities. Accessory minerals are zircon, apatite, epidote, rutile, and opaque phases. This lithotype occurs in the sections Brezovica II, Donji Kamenečki I and XI, and Golubovec (Fig. 3).

*Crystalloclastic tuffs* are composed of coarse ash to lapilli-sized pyroclastic material (Fig. 4i). Dominant crystalloclasts are quartz, plagioclase, and K-feldspars, with less pleochroic mica. The variable size crystalloclasts of quartz are angular showing a jig-saw fit texture and, sporadically, the oval-spherical cavities typical for volatile-rich systems (Fig. 4j). The crystalloclasts of plagioclase ($An_{21.3\text{-}55.3}Ab_{40.9\text{-}77.7}Or_{1.1\text{-}3.8}$) and K-feldspar ($An_{0.1\text{-}3.8}Ab_{1.6\text{-}26.4}Or_{72.71\text{-}98.4}$; Fig. 5; Table 1) have mainly subhedral to euhedral shapes. Pumice fragments and lithoclasts are also present (Fig. 4i).

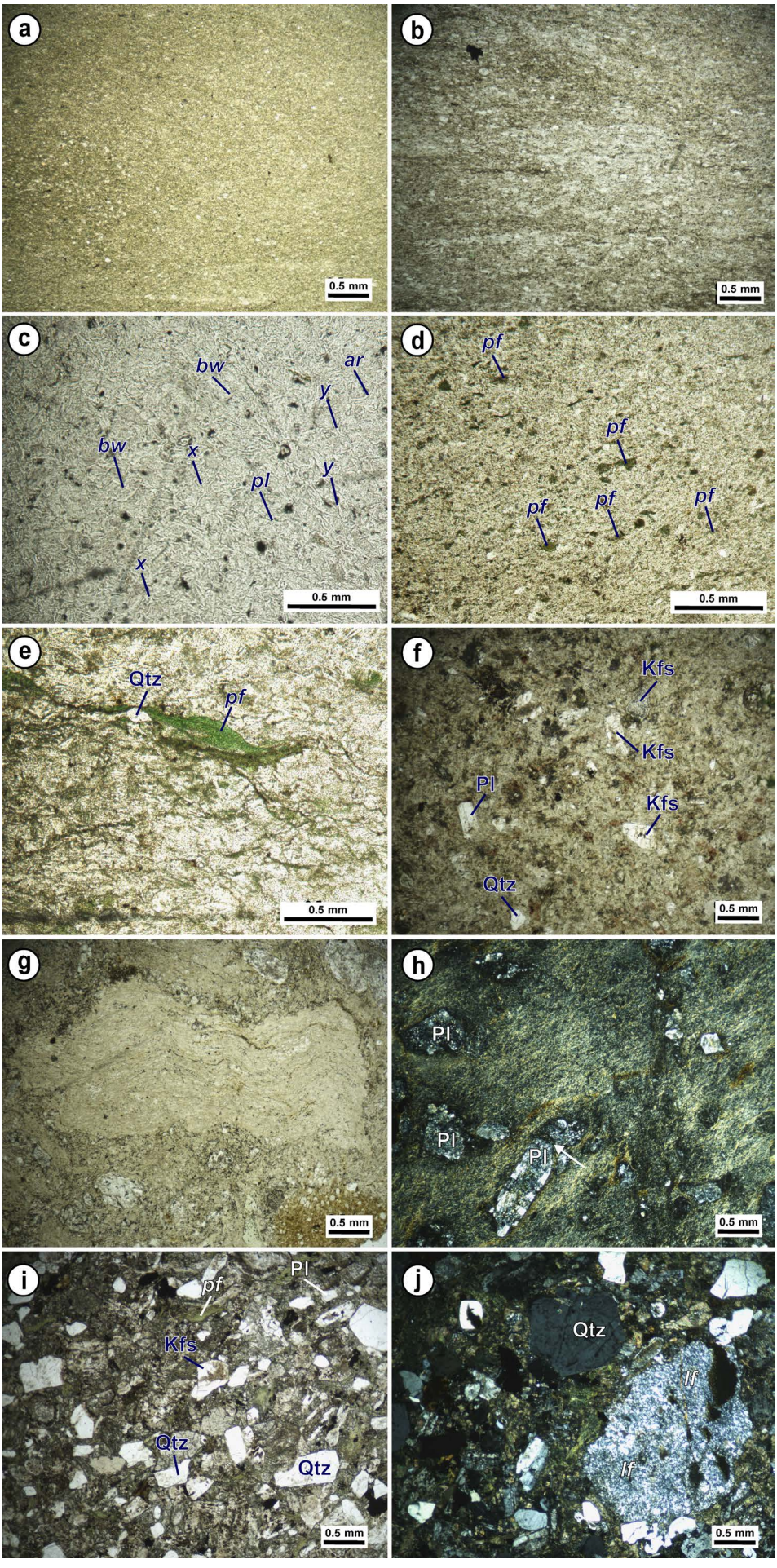


Fig. 4 - Micropetrographical characteristics of the Middle Triassic acidic pyroclastic rocks from the Kuna Gora, Strahinjščica and Ivanščica Mts. a) Homogenous vitroclastic (VC) tuff composed of fine ash particles (sample DK XI - 3.60); b) VC tuff composed of fine ash particles exhibiting faint horizontal lamination visible due to change of alteration products resulting in colour differences (sample BR I - 7.80); c) VC tuff composed of medium sized glass shards with various shapes (sample GK I - 12.10): *x* = x shaped, *y* = y shaped, *pl* = platy, *ar* = arcuate, *bw* = bubble wall shards; d) Pumice fragments up to 0.25 mm and completely devitrified to chlorite in the VC tuff lithotype; pf = pumice fragment (sample KG III - 11.30); e) Pumice fragment completely altered to chlorite aggregate, and squeezed and plasticly deformed with the fine quartz crystaloclast embedded into the pumice fragment (sample DK XI - 5.70): *pf* = pumice fragment; f) Crystalloclastic particles found in VC tuff are commonly altered feldspars and quartz. Sample DK I - 3.70 exhibits rare unaltered feldspar crystalloclast; g) Lapilli sized pumice fragments found in vitro crystalloclastic (VCC) tuff (sample BR II - 27.20); h) Feldspar crystalloclasts in VCC tuff (sample BR II - 23.20). Arrow pointing to the jig-saw fit crystalloclast structure; i) Crystalloclastic (CC) tuffs are composed mainly of quartz, alkali feldspar and plagioclase crystalloclasts (sample SEK - 13.55/3): *pf* = pumice fragment; j) Quartz with oval cavities and certain amount of lithoclasts in the volatile rich systems. Sample SEK - 13.55/2 exhibits a vitroclastic tuff lithoclast of lapilli size: *lf* = lithoclast. Matrix is composed of fine ash devitrified to chlorite, microcrystalline quartz, clay minerals, opaque minerals. Mineral abbreviations after Kretz (1983): Kfs = alkali feldspar, Pl = plagioclase, Qtz = quartz.

Table 1 - Representative chemical compositions and calculated mineral formulae of alkali-feldspar and plagioclase from the rhyolitic tuffs from the Kuna Gora, Strahinjščica and Ivanščica Mts.

| Mineral | Alkali feldspar | | | | | | Plagioclase | | | | | | |
|---|---|---|---|---|---|---|---|---|---|---|---|---|---|
| Sample | DK I-3.70 | SEK-13.55 | SEK-13.55 | SER-13.55 | SEK-13.55 | SEK-13.55 | DK I-3.70 | DK I-3.70 | DK I-3.70 | SEK-13.55 | SEK-13.55 | SEK-13.55 | SEK-13.55 |
| Lithotype | VCC | CC | CC | CC | CC | CC | VCC | VCC | VCC | CC | CC | CC | CC |
| Anal. No. | 4 | 7 | 11c | 12r | 15 | 22 | 5 | 8 | 22 | 13 | 17c | 18r | 19r |
| Species | *sa* | *sa* | *sa* | *sa* | *sa* | *sa* | *ab* | *ab* | *ab* | *la* | *ol* | *la* | *an* |
| Oxides (wt.%) | | | | | | | | | | | | | |
| $SiO_2$ | 69.58 | 67.80 | 66.01 | 66.36 | 66.38 | 66.85 | 57.35 | 66.87 | 66.28 | 53.54 | 62.02 | 53.92 | 57.35 |
| $TiO_2$ | 0.01 | 0.00 | 0.00 | 0.00 | 0.00 | 0.01 | 0.00 | 0.00 | 0.06 | 0.00 | 0.03 | 0.00 | 0.00 |
| $Al_2O_3$ | 16.59 | 17.59 | 19.01 | 19.04 | 18.19 | 17.71 | 27.44 | 21.16 | 20.84 | 28.91 | 23.90 | 29.04 | 27.44 |
| FeO | 0.43 | 0.008 | 0.05 | 0.02 | 0.03 | 0.29 | 0.29 | 0.17 | 0.46 | 0.34 | 0.09 | 0.34 | 0.29 |
| MnO | 0.01 | 0.02 | 0.00 | 0.00 | 0.00 | 0.04 | 0.00 | 0.00 | 0.01 | 0.00 | 0.01 | 0.02 | 0.00 |
| MgO | 0.17 | 0.003 | 0.00 | 0.01 | 0.01 | 0.11 | 0.00 | 0.00 | 0.14 | 0.03 | 0.00 | 0.00 | 0.00 |
| CaO | 0.05 | 0.07 | 0.17 | 0.17 | 0.01 | 0.72 | 8.84 | 2.02 | 1.80 | 10.78 | 4.68 | 11.01 | 8.84 |
| $Na_2O$ | 0.43 | 0.21 | 2.25 | 2.87 | 0.17 | 0.88 | 6.43 | 11.00 | 10.88 | 4.40 | 9.44 | 5.08 | 6.43 |
| $K_2O$ | 13.28 | 15.03 | 12.80 | 11.98 | 16.01 | 14.02 | 0.54 | 0.08 | 0.10 | 0.62 | 0.19 | 0.50 | 0.54 |
| Total | 100.56 | 100.84 | 100.28 | 100.45 | 100.80 | 100.64 | 100.89 | 101.30 | 100.56 | 98.62 | 100.36 | 99.93 | 100.89 |
| Calculated mineral formulae (a.p.f.u.) | | | | | | | | | | | | | |
| Si | 3.126 | 3.070 | 2.997 | 2.999 | 3.028 | 3.038 | 2.556 | 2.905 | 2.903 | 2.451 | 2.745 | 2.445 | 2.556 |
| Ti | 0.000 | 0.000 | 0.000 | 0.000 | 0.000 | 0.000 | 0.000 | 0.000 | 0.002 | 0.000 | 0.001 | 0.000 | 0.000 |
| $Al_{tot}$ | 0.878 | 0.938 | 1.016 | 1.013 | 0.977 | 0.948 | 1.440 | 1.082 | 1.075 | 1.559 | 1.246 | 1.556 | 1.440 |
| $Fe^{2+}$ | 0.016 | 0.003 | 0.002 | 0.001 | 0.001 | 0.011 | 0.011 | 0.006 | 0.017 | 0.013 | 0.004 | 0.013 | 0.011 |
| Mn | 0.000 | 0.001 | 0.000 | 0.000 | 0.000 | 0.000 | 0.000 | 0.000 | 0.000 | 0.000 | 0.000 | 0.000 | 0.000 |
| Mg | 0.012 | 0.002 | 0.000 | 0.001 | 0.001 | 0.000 | 0.000 | 0.000 | 0.009 | 0.002 | 0.000 | 0.000 | 0.000 |
| Ca | 0.053 | 0.004 | 0.008 | 0.008 | 0.000 | 0.035 | 0.422 | 0.094 | 0.084 | 0.529 | 0.222 | 0.535 | 0.422 |
| Na | 0.037 | 0.019 | 0.198 | 0.251 | 0.015 | 0.078 | 0.556 | 0.926 | 0.924 | 0.391 | 0.810 | 0.446 | 0.556 |
| K | 0.761 | 0.868 | 0.741 | 0.691 | 0.932 | 0.813 | 0.031 | 0.005 | 0.006 | 0.971 | 0.011 | 0.029 | 0.031 |
| Total | 4.833 | 4.905 | 4.962 | 4.964 | 4.954 | 4.921 | 5.016 | 5.018 | 5.020 | 4.981 | 5.039 | 5.017 | 5.016 |
| An | 0.37 | 0.45 | 0.84 | 0.84 | 0.01 | 3.78 | 2.42 | 9.17 | 8.28 | 55.33 | 21.28 | 52.97 | 41.82 |
| Ab | 4.62 | 2.13 | 20.91 | 26.42 | 1.57 | 8.42 | 90.89 | 90.34 | 91.12 | 40.90 | 77.66 | 44.16 | 55.10 |
| Or | 95.00 | 97.40 | 78.20 | 72.70 | 98.40 | 87.80 | 6.70 | 0.50 | 0.60 | 3.80 | 1.10 | 2.90 | 3.10 |

Formulae calculated on the basis of 8 oxygens and total Fe as divalent for K-feldspar and plagioclase; VCC = vitrocrystalloclastic tuff; CC = crystalloclastic tuff; c = core, r = rim; *ab* = albite, *an* = andesine; *la* = labradorite; *ol* = oligoclase, *sa* = sanidine. An = 100*Ca/(Ca+ N +K).

Table 2 - Distribution and XRD/EMPA relative abundances of primary and alteration phases in rhyolitic tuffs from the Kuna Gora, Strahinjščica and Ivanščica Mts.

| Sample | Litho -type | **Qtz** | **Kfs** | **Pl** | **Ab** | **MFe** | **MAl** | **MNa** | **Kln** | **I-S** | **Zeo** | **Am** | **Jar** | **Cpx** | **Ilv** | **Cal** | **Pmp** | **Ilm** | **Hm** |
|---|---|---|---|---|---|---|---|---|---|---|---|---|---|---|---|---|---|---|---|
| BR-10.60 | *VC* | ++ | | | | | + | | + | * | + | | | | | | | | |
| BR-24.50 | *VC* | ++ | | | | | + | | + | + | | * | + | | | | | | |
| BRII-13.85 | *VC* | ++ | + | | + | + | | | + | * | + | | | | | | | | |
| BRII-20.40 | *VCC* | ++ | + | | + | + | | | + | * | | | | | | | | | |
| DKI-0.40 | *VC* | ++ | + | | + | + | | | * | * | * | | | * | | | | | |
| DKI-3.30 | *VCC* | ++ | + | | + | + | | | * | * | * | | | | | | | | |
| DKI-3.70 | *VCC* | x | x | x | x | | | x | x | | | | | | | | | | |
| DKXI-3.60 | *VC* | ++ | + | | + | + | | | * | * | | | | | | | | | |
| DKXI-5.10 | *VCC* | ++ | + | | + | + | | | + | * | | | | | * | | | | |
| DK-III | *VC* | ++ | + | | + | + | | | * | * | | | | | | | | | |
| DK-V | *CC* | ++ | + | | + | | + | | * | * | * | | | | | | | | |
| DK-VIII | *VCC* | ++ | + | | + | | + | | | + | | | | | | | | | |
| GKI-12.10 | *VC* | ++ | + | | + | | + | | | | | | | | | | | | + |
| GKII-11.50 | *VC* | ++ | * | | ++ | + | * | | + | | | | | | | ++ | | | |
| GO-16.10 | *VC* | ++ | + | | + | + | * | | | | | | | | | | | | |
| GO-17.50 | *CC* | ++ | + | | ++ | + | * | | | | | | | | | | | | |
| KGIII-6.40 | *VC* | ++ | * | | + | + | | | + | + | * | | | | | | | | |
| KGIII-10.75 | *VC* | ++ | | | + | | + | | * | | | | | * | | | | | |
| SEK-13.55 | *CC* | x | x | x | x | x | | | | x | | | | | | | | x | |
| SEK-15.25 | *VCC* | ++ | + | | + | | + | | | * | | | | | | | * | | |
| SEK-37.35 | *VC* | ++ | | | + | + | * | | | | | | | | | | + | | |

Abbreviations: Ab = albite; Am = amphibole; Cal = calcite; Cpx = clinopyroxene; Hm = hematite; Ilv = ilvaite; Ilm = ilmenite; I-S = illite-smectite; Jar = jarosite; Kfs = K-feldspar; Kln = kaolinite; MFe = Fe-Mg mica; MAl = Al mica; MNa = Na mica; Qtz = quartz; Pl = plagioclase; Pmp = pumpellyite; Zeo = zeolite; ++ = indicates major phases, + = indicates minor phases, * = indicates phases present, but not unequivocally confirmed by XRD, x = indicates phases detected by EMPA in samples not measured by XRD. Mineral abbreviations after Kretz (1983). VC = vitroclastic tuff; VCC = vitrocrystalloclastic tuff; CC = crystalloclastic tuff.

The latter are determined as carbonate, tuff and chert. Modal composition of this lithotype is determined as quartz 40 vol%, plagioclase 20 vol%, K-feldspar 15 vol%, pumice fragments 10 vol% and lithoclasts 15 vol%. The matrix of the crystalloclastic tuffs is made of fine ash devitrified to chlorite, microcrystalline quartz, clay minerals and opaque minerals (Fig. 4j, Table 2), with sporadical carbonate domains. This lithotype is present in Sekolje section (SEK–13.55) and Brezovica II section (BR II-7.05; Fig. 3).

The X-ray diffraction data showed that quartz is an omnipresent constituent of studied tuffs while K-feldspar and albite commonly occur (Table 2). The latter must be related to the alteration of plagioclase. Similar to feldspar, mica is also present in most of the studied samples. Its composition is however twofold; it is either an Al-rich variety, likely muscovite, or Fe-Mg rich member of the illite-alumoceladonite series. The former may be a crystalloclast while the latter stands for a final stage of evolution of the glassy component occasionally dominating the sample characterized with an intensive yellowish to greenish colour and parallel to subparallel cleavage. Corresponding alteration parageneses are reported by Slovenec et al. (2020) in intermediate tuffs of the mid-Triassic volcano-sedimentary succession of the neighboring Ivanščica Mt. Only exceptionally paragonite-type mica has been documented thanks to the EMPA investigation (Table 2). Illite-smectite which is rarely present likely represents a low-temperature weathering product (Cuadros et al., 1999), while kaolinite, zeolite, jarosite, pumpellyite, and possibly ilvaite are attributed to low-grade hydrothermal event(s) (Ertek and Öner, 2008; Donoghue et al., 2008; Arbiol et al., 2021).

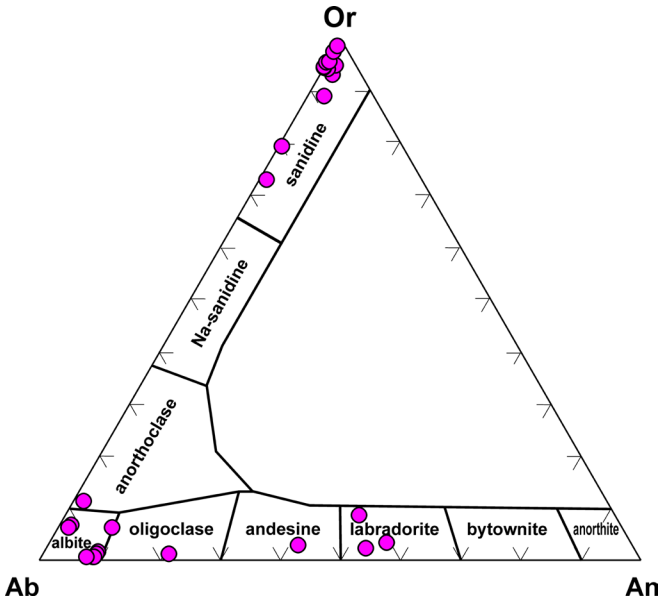


Fig. 5 - Classification diagrams for feldspar [Ab - An - Or plot; Deer et al., 1992; Dana et al., 1993] from the acidic pyroclastic rocks from the Kuna Gora, Strahinjščica and Ivanščica Mts.

### Bulk-rock chemistry of *Pietra Verde* tuffs

The chemical composition of representative rock samples is shown in Table 3. The investigated pyroclastic rocks are characterized by a high $SiO_2$ content exceeding 71.47 wt%. Only two VCC samples show slightly lower silica values ($SiO_2$ = 64.73-69.72 wt%). All samples are characterized by moderately high $Al_2O_3$ (up to 15.41 wt%) and a low content of $TiO_2$ (≤ 0.38 wt%), $Fe_2O_3$ (≤ 3.76 wt%), MgO (0.35-2.10 wt%), and $P_2O_5$ (≤ 0.10 wt%), while potassium concentrations span a large range (1.64-7.66 wt%). As per Winchester and Floyd (1977), a high $Zr/TiO_2$ ratio (554-1354) with moderate Nb/Y values (0.17-0.65) is indicative for subalkaline rhyolite (Fig. 6a, b). This is corroborated by low Nb-Ta values (Nb < 16.7 ppm, Ta < 1.2 ppm; after Tian et al., 2010). The high values of Ce/Yb (10.31-31.51) and

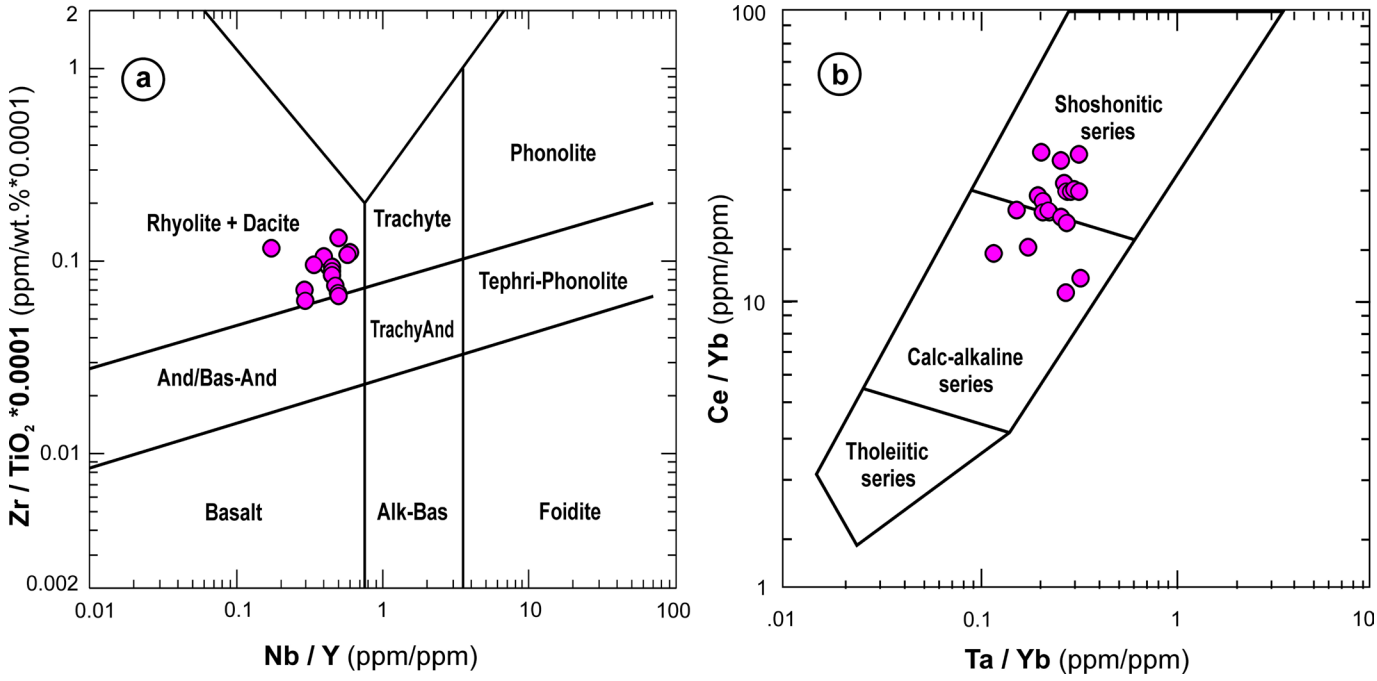


Fig. 6 - a) Nb/Y - $Zr/TiO_2*10^{-4}$ classification diagram (Winchester and Floyd, 1977) and, b) Ce/Yb - Ta/Yb discrimination diagram after Pearce (1982) for the acidic pyroclastic rocks from the Kuna Gora, Strahinjščica and Ivanščica Mts.

Table 3 - Chemical compositions of rhyolitic tuffs from the Kuna Gora, Strahinjščica and Ivanščica Mts.

| | Kuna Gora Mt. | | | Strahinjščica Mt. | | | | | | | | | | | | | | Ivanščica Mt. |
|---|---|---|---|---|---|---|---|---|---|---|---|---|---|---|---|---|---|---|
| Sample | KG III-2.20 | KG III-6.40 | KG III-11.30 | BR I-7.80 | BR I-24.50 | BR II-15.45 | BR II-23.20 | GK I-12.10 | GK I-19.00 | GK II-2.80 | GK III-0.50 | DK I-1.90 | DK XI-3.60 | DK XI-5.70 | DK XI-20.80 | SEK-6.75 | SEK-15.25 | SEK-37.35 | GO-15.50 |
| Sample loc. | 1 | 1 | 1 | 2 | 2 | 3 | 3 | 4 | 4 | 5 | 6 | 7 | 8 | 8 | 8 | 9 | 9 | 9 | 10 |
| Lithotype | VC | VC | VC | VC | VC | VCC | VCC | VC | VC | VC | VC | VC | VC | VC | VCC | VC | VCC | VC | VCC |
| $SiO_2$ | 74.64 | 74.91 | 74.03 | 80.18 | 73.09 | 72.26 | 69.77 | 73.82 | 77.94 | 74.06 | 72.80 | 72.95 | 71.47 | 73.72 | 73.46 | 72.51 | 64.73 | 72.47 | 73.53 |
| $TiO_2$ | 0.15 | 0.14 | 0.11 | 0.34 | 0.33 | 0.16 | 0.17 | 0.21 | 0.18 | 0.16 | 0.22 | 0.20 | 0.21 | 0.24 | 0.14 | 0.16 | 0.38 | 0.11 | 0.17 |
| $Al_2O_3$ | 10.84 | 12.21 | 10.52 | 7.28 | 13.45 | 13.21 | 14.52 | 11.97 | 10.32 | 12.07 | 10.53 | 10.98 | 13.40 | 12.71 | 12.76 | 11.51 | 15.41 | 12.35 | 13.82 |
| $Fe_2O_{3total}$ | 2.02 | 1.53 | 2.81 | 1.61 | 1.65 | 2.01 | 2.34 | 3.02 | 0.12 | 1.05 | 3.12 | 2.93 | 1.85 | 1.39 | 1.31 | 3.18 | 3.76 | 2.01 | 2.28 |
| MnO | 0.06 | 0.02 | 0.09 | 1.78 | 0.11 | 0.07 | 0.06 | 0.03 | 0.04 | 0.03 | 0.02 | 0.03 | 0.09 | 0.02 | 0.04 | 0.06 | 0.07 | 0.02 | 0.02 |
| MgO | 1.04 | 1.15 | 1.22 | 1.25 | 1.68 | 1.82 | 2.10 | 0.49 | 0.47 | 0.44 | 0.51 | 0.49 | 0.81 | 0.80 | 0.81 | 1.39 | 1.69 | 1.81 | 0.35 |
| CaO | 0.32 | 0.19 | 0.11 | 0.03 | 0.12 | 0.09 | 0.11 | 0.71 | 0.86 | 0.42 | 0.54 | 0.48 | 0.26 | 0.22 | 0.23 | 0.36 | 2.07 | 3.17 | 0.19 |
| $Na_2O$ | 4.45 | 3.85 | 5.15 | bdl | 3.09 | 2.16 | 1.51 | 1.31 | 0.28 | 2.29 | 2.22 | 1.28 | 2.42 | 4.26 | 3.65 | 0.03 | 1.06 | 1.00 | 4.88 |
| $K_2O$ | 1.96 | 1.64 | 2.16 | 2.14 | 2.21 | 3.44 | 4.42 | 7.06 | 7.56 | 5.96 | 6.05 | 6.95 | 6.02 | 2.18 | 3.27 | 7.66 | 5.90 | 3.22 | 3.23 |
| $P_2O_5$ | 0.02 | 0.03 | 0.03 | 0.04 | 0.03 | 0.03 | 0.03 | 0.05 | 0.07 | 0.06 | 0.04 | 0.05 | 0.10 | 0.02 | 0.02 | 0.03 | 0.06 | 0.03 | 0.03 |
| LOI | 3.98 | 2.55 | 3.23 | 3.39 | 3.21 | 2.80 | 3.44 | 0.35 | 1.09 | 2.31 | 3.65 | 2.48 | 1.43 | 1.24 | 1.46 | 2.19 | 3.10 | 2.65 | 1.40 |
| Total | 99.48 | 98.22 | 99.45 | 98.04 | 98.97 | 98.06 | 98.47 | 99.20 | 98.94 | 98.85 | 99.70 | 98.82 | 98.06 | 96.80 | 97.15 | 99.08 | 98.23 | 98.84 | 99.00 |
| Cs | 1.6 | 1.8 | 0.3 | 5.0 | 4.4 | 3.5 | 4.9 | 1.0 | 0.3 | 0.8 | 1.2 | 1.2 | 2.1 | 1.6 | 2.8 | 7.5 | 4.5 | 3.4 | 1.5 |
| Rb | 49 | 52 | 6 | 83 | 71 | 131 | 161 | 118 | 109 | 102 | 121 | 111 | 133 | 91 | 136 | 191 | 167 | 116 | 92 |
| Ba | 158 | 129 | 82 | 744 | 821 | 161 | 215 | 502 | 548 | 529 | 435 | 552 | 530 | 307 | 401 | 364 | 988 | 378 | 582 |
| Th | 13.3 | 12.4 | 11.2 | 5.9 | 6.4 | 17.9 | 18.1 | 15.7 | 14.7 | 13.8 | 16.0 | 15.3 | 14.8 | 17.0 | 17.8 | 15.9 | 18.5 | 15.1 | 16.3 |
| Ta | 0.77 | 0.93 | 0.82 | 0.58 | 0.57 | 1.04 | 1.01 | 0.69 | 0.61 | 0.59 | 0.72 | 0.66 | 0.95 | 0.90 | 0.94 | 0.82 | 1.15 | 0.81 | 1.10 |
| Nb | 11.3 | 11.9 | 12.0 | 10.0 | 10.1 | 13.9 | 14.4 | 9.3 | 9.5 | 10.0 | 9.4 | 9.6 | 13.6 | 11.8 | 12.9 | 11.8 | 15.7 | 11.2 | 13.3 |
| Sr | 128 | 149 | 122 | 76 | 117 | 29 | 27 | 43 | 56 | 61 | 38 | 46 | 42 | 93 | 142 | 66 | 256 | 118 | 116 |
| Zr | 136 | 133 | 104 | 188 | 193 | 179 | 192 | 143 | 158 | 171 | 145 | 152 | 275 | 161 | 176 | 217 | 270 | 132 | 167 |
| Hf | 4.3 | 4.4 | 3.7 | 3.1 | 4.4 | 5.5 | 5.7 | 4.2 | 4.4 | 4.6 | 4.0 | 4.2 | 7.4 | 5.2 | 5.5 | 6.0 | 7.8 | 4.6 | 5.9 |
| Y | 25.8 | 28.6 | 27.3 | 32.1 | 34.3 | 23.8 | 25.3 | 19.1 | 21.6 | 25.7 | 18.9 | 20.7 | 47.1 | 5.2 | 36.3 | 24.3 | 5.1 | 66.7 | 40.3 |
| Sc | 12 | 13 | 14 | 11 | 12 | 13 | 13 | 7 | 6 | 9 | 8 | 9 | 14 | 11 | 11 | 11 | 17 | 12 | 14 |
| V | 30 | 28 | 25 | 69 | 66 | 27 | 30 | 32 | 35 | 32 | 32 | 33 | 34 | 26 | 25 | 31 | 55 | 32 | 14 |
| Cr | 10 | 10 | 11 | 37 | 32 | 7 | 8 | 10 | 11 | 13 | 10 | 11 | 11 | 8 | 10 | 12 | 16 | 10 | 21 |
| Ni | 9 | 9 | 13 | 45 | 43 | 7 | 9 | 7 | 8 | 9 | 7 | 7 | 13 | 5 | 7 | 24 | 9 | 8 | 3 |
| Pb | 11.4 | 14.2 | 6.8 | 26.7 | 32.2 | 8.2 | 21.0 | 5.2 | 8.7 | 16.2 | 4.8 | 6.6 | 10.9 | 11.2 | 32.6 | 3.7 | 5.5 | 46.3 | 17.5 |
| U | 2.37 | 2.12 | 2,25 | 2.04 | 2.10 | 5.15 | 5.13 | 5.06 | 5.31 | 3.28 | 2.95 | 2.18 | 3.57 | 2.05 | 3.33 | 0.80 | 1.99 | 5.15 | 2.62 |
| La | 25.23 | 34.57 | 24.51 | 26.44 | 35.21 | 18.58 | 48.75 | 28.34 | 31.91 | 35.32 | 26.44 | 29.31 | 32.37 | 19.01 | 41.09 | 34.34 | 60.73 | 51.50 | 63.93 |
| Ce | 53.02 | 73.88 | 52.31 | 53.01 | 71.24 | 38.28 | 88.80 | 52.01 | 66.91 | 87.90 | 50.91 | 53.18 | 77.44 | 31.18 | 76.78 | 76.44 | 103.73 | 95.50 | 21.52 |
| Pr | 6.74 | 8.13 | 5.72 | 6.59 | 7.95 | 4.29 | 13.17 | 5.49 | 6.77 | 9.03 | 5.29 | 5.74 | 8.09 | 4.16 | 8.32 | 7.82 | 13.80 | 13.42 | 15.67 |
| Nd | 24.22 | 31.29 | 22.52 | 27.31 | 30.73 | 16.16 | 52.78 | 19.02 | 24.70 | 32.89 | 18.62 | 20.07 | 32.23 | 14.81 | 30.95 | 30.25 | 54.03 | 50.73 | 57.80 |
| Sm | 5.25 | 6.96 | 5.13 | 6.02 | 7.14 | 3.21 | 10.31 | 3.87 | 4.50 | 7.43 | 3.58 | 4.03 | 6.91 | 2.79 | 5.75 | 6.30 | 11.40 | 11.45 | 11.31 |
| Eu | 0.56 | 0.70 | 0.61 | 1.25 | 1.36 | 0.22 | 0.70 | 0.54 | 0.47 | 0.59 | 0.52 | 0.55 | 0.80 | 0.20 | 0.41 | 0.55 | 1.52 | 1.04 | 1.20 |
| Gd | 5.38 | 6.52 | 5.40 | 6.66 | 7.76 | 2.99 | 6.69 | 4.42 | 3.91 | 5.97 | 3.92 | 4.68 | 7.18 | 2.38 | 5.96 | 6.18 | 11.17 | 10.74 | 9.57 |
| Tb | 0.77 | 0.93 | 0.80 | 0.97 | 1.06 | 0.50 | 0.92 | 0.64 | 0.57 | 0.97 | 0.56 | 0.69 | 1.17 | 0.42 | 0.90 | 0.92 | 1.70 | 1.80 | 1.57 |
| Dy | 4.98 | 5.74 | 5.19 | 5.92 | 6.96 | 3.60 | 5.27 | 3.97 | 3.57 | 5.03 | 3.59 | 4.32 | 8.18 | 2.91 | 6.05 | 5.34 | 10.84 | 12.44 | 7.91 |
| Ho | 1.02 | 1.11 | 1.08 | 1.14 | 1.31 | 0.89 | 1.04 | 0.74 | 0.73 | 0.93 | 0.71 | 0.86 | 1.81 | 0.70 | 1.29 | 1.00 | 2.12 | 2.53 | 1.46 |
| Er | 3.21 | 3.29 | 3.24 | 3.11 | 3.62 | 3.21 | 3.36 | 2.29 | 2.25 | 2.69 | 2.31 | 2.33 | 5.69 | 2.37 | 3.98 | 2.66 | 6.11 | 7.50 | 3.42 |
| Tm | 0.43 | 0.48 | 0.45 | 0.42 | 0.57 | 0.51 | 0.53 | 0.32 | 0.33 | 0.39 | 0.29 | 0.38 | 0.81 | 0.38 | 0.59 | 0.37 | 0.81 | 1.02 | 0.47 |
| Yb | 2.84 | 3.20 | 2.92 | 2.72 | 3.59 | 3.71 | 3.63 | 2.21 | 2.28 | 2.79 | 2.20 | 2.32 | 5.28 | 2.70 | 4.01 | 2.48 | 5.37 | 6.77 | 2.68 |
| Lu | 0.44 | 0.48 | 0.45 | 0.40 | 0.52 | 0.58 | 0.55 | 0.37 | 0.35 | 0.37 | 0.32 | 0.36 | 0.83 | 0.43 | 0.61 | 0.35 | 0.74 | 0.93 | 0.35 |

Major elements in wt.%, trace elements in ppm. LOI = loss on ignition at 1100oC. bdl = below detection limit. Sample location number corresponds to the locations in Figure 2. VC = vitroclastic tuff; VCC = vitrocrystalloclastic tuff.

Ta/Yb (0.12-0.33) indicate rocks' middle to high-K calc-alkaline and shoshonitic affinity (Fig. 6b). Low Ni ≤ 45 ppm and Cr ≤ 37 ppm are consistent with the nature of these evolved acidic rocks (e.g., Wilson, 1989). A wide range of concentrations of large ion lithophile elements (LILE) such as Cs, Rb, K and Ba, as well as moderately high content of Loss On Ignation value (up to 3.98 wt%) indicate their mobilization due to secondary alterations which is consistent with the petrographic observation and will therefore not be used in petrogenetic considerations. The above also applies to most of the major elements. Unlike them, high field strength elements (HFSE) such as Th, Nb, Ta, Ti, Hf, P, Y, and rare earth elements (REE) most probably remained immobile (Pearce and Norry, 1979; Pearce, 1982; Rollinson, 1993; Table 3).

The multielement concentration patterns normalized to primitive mantle are displayed in Fig. 7a1, a2. The samples show secondary enrichment in LILE (e.g., Cs, Rb, K) and Th (up to 940 times relative to PM), strong negative anomaly of HFSE (Nb-Ta, P, Ti) and variable positive Pb [$(Pb/Ce)_{PMN}$ = 1.20-12.61] spikes. Such anomalies can be attributed to apatite fractionation (P depletion) and Fe-Ti oxide (Ti depletion), crustal contamination (Pb enrichment) and impact of the subducted crust (Nb-Ta depletion; e.g., Pearce et al., 1984; Hofmann, 1997).

The chondrite-normalized rare earth elements (REE) patterns are shown in Fig. 7b1, b2. All samples show the light rare earth elements (LREE) fractionation and enrichment [$(La/Lu)_{CN}$ = 3.33-10.19] at 23-180 times chondrite relative concentrations and relatively weakly fractionated approximately flat pattern of heavy rare earth elements (HREE) [$(Tb/Lu)_{CN}$ = 0.57-1.73] at 23-36 times relative to chondrite. The high concentrations of LREE likely indicate the presence of zircon, apatite and titanite in which these elements are readily hosted. The occurrence of a significant negative Eu anomaly (Eu/Eu* = 0.21-0.59) in all samples may reflects crustal signature and/or removal of feldspar from acidic magmas and indicates fractional crystallization of plagioclase as an important process in the genesis of the analyzed acidic pyroclastic rocks (e.g., Rollinson, 1993; Rudnik and Gao, 2014).

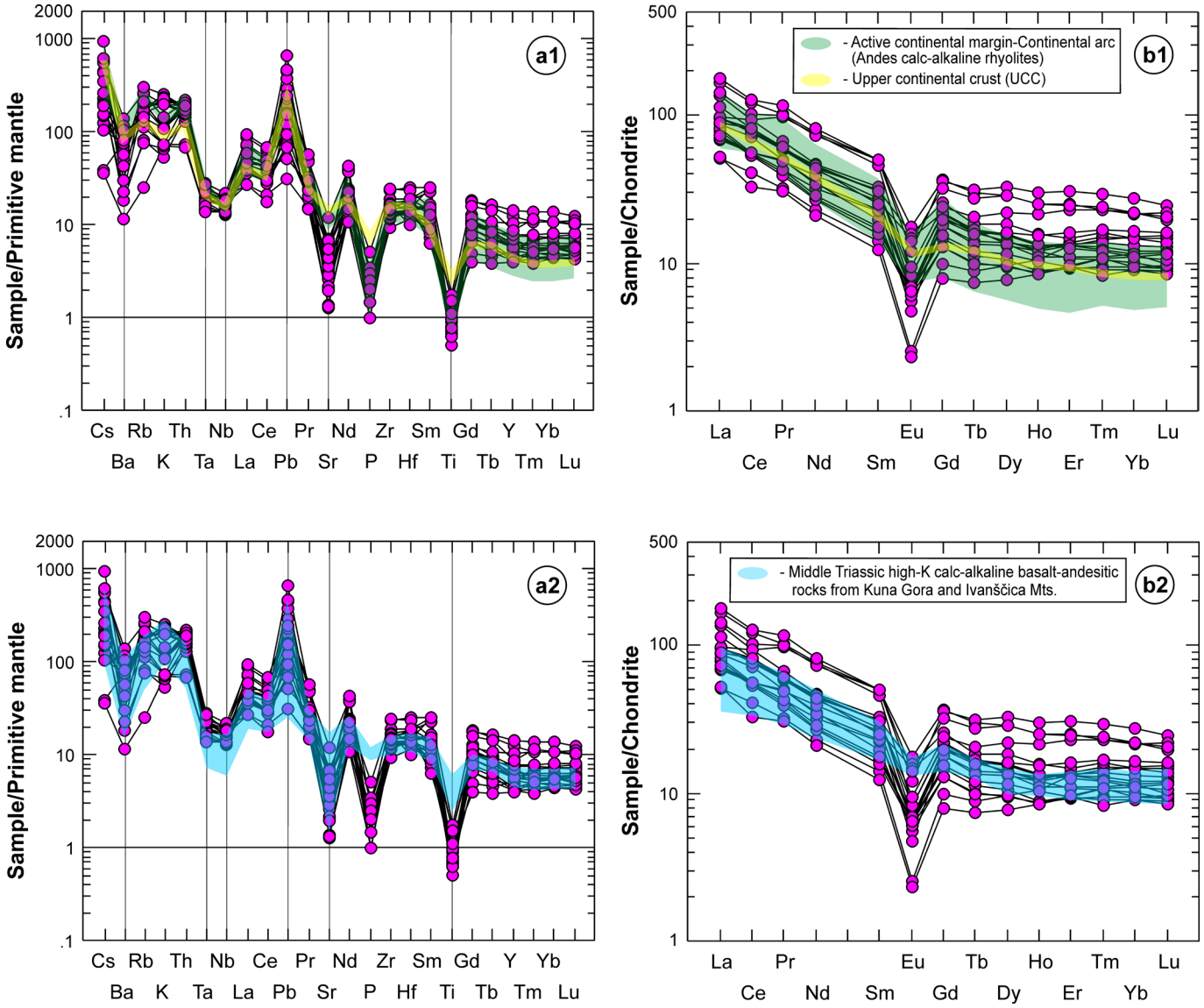


Fig. 7 a1), a2) Primitive mantle-normalised multielement and (b1), b2) REE patterns for the acidic pyroclastic rocks from the Kuna Gora, Strahinjščica and Ivanščica Mts. Normalisation values are from Sun and McDonough (1989) and Taylor and McLennan (1985). Pattern for upper continental crust (UCC; Rudnick and Gao, 2014), Andes calc-alkaline rhyolites (Riley et al., 2001; Garrison et al., 2011) and Middle Triassic high-K calc-alkaline basalt-andesitic rocks from Kuna Gora and Ivanščica Mts. (Slovenec et al., 2020; Slovenec and Šegvić, 2021) are plotted for correlation constrains.

The neodymium isotope composition of analyzed rocks is shown in Table 4. The values of $^{143}Nd/^{144}Nd$ of six representative samples vary in a relatively narrow range from 0.512288 to 0.512344. The initial εNd are calculated for 244 Ma, which is the average estimated time of volcanic activity and deposition of analyzed acidic pyroclastic rocks obtained based on their biostratigraphic position in the recorded geological columns (Fig. 3; Kukoč et al., in review). The initial $\varepsilon_{Nd}$ varies between -2.71 to -4.95. Low initial $^{143}Nd/^{144}Nd$ and $\varepsilon_{Nd(t)}$ values close to the subducted continental material field, suggest a high degree of crustal contamination (Fig. 8).

## DISCUSSION

### Petrogenesis of *Pietra Verde* tuffs

The origin of Middle Triassic acidic vitroclastic, crystalloclastic, and vitrocrystaloclastic high-K, calc-alkaline to shoshonitic tuffs from NW Croatia is attributed to pyroclastic density flows and surges as well as the distal airborn transport (Kukoč et al., in review). Such a lithological association offers a wealth of information about the crust and mantle geochemistry (e.g., Peccerillo and Taylor, 1976; Halder et al., 2021). Rhyolitic eruptions are typical in a continental setting being often related to partial melting of the continental crust coupled with magma differentiation, fractional crystallization, and crustal assimilation (e.g., Wilson, 1989; Halder et al., 2021). Considering that studied rhyolitic rock is altered to a certain degree, suggested petrogenetic sequences has been attested on the basis of discrimination ratios of immobile trace elements and the Nd isotopic data. Low values of Nb* and Ta* ratios (Fig. 9) as well as very similar multielement and REE patterns (Fig. 7a2, b2) are strongly consistent with a notation on their source magmas which were apparently derived from basaltic-andesitic lavas which furthermore produced pyroclastic rocks of the same Middle Triassic age cropping out at Ivanščica and Kuna Gora Mts (Slovenec et al., 2020; Slovenec and Šegvić, 2021). The negative anomalies of the Nb-Ta pair in the studied acid pyroclastic rocks suggest the influence of subducted crust (Fig. 7a1). The crustal component, i.e., the strong influence of subducted/recycled sediments is indicated by: i) negative values of initial $\varepsilon_{Nd}$ (-2.71 to -4.95) accompanied by the low values of $^{147}Sm/^{144}Nd$ ratio (≤ 0.136566; Fig. 8a) and, ii) an increasing Th/La at constant Sm/La ratio trend (0.14-0.22) (Fig. 8b). However, apart from the subducted sediments involved in the generation of the magmas, the formation of the studied acidic rocks most likely involves melting of crustal rocks. The chondrite-normalized REE patterns similar to those of the average upper continental crust (Fig. 7b1), as well as positive anomaly of Pb observed in the primitive mantle normalized patterns (Fig. 7a1) are characteristic of acidic magmas whose origin is related to partial melting of the upper continental crust (Wilson, 1989). In addition to partial melting, the formation of studied rocks must have included fractional crystallization. Prominent negative anomalies of Sr (Fig. 7a1) are indicative for plagioclase and K-feldspar fractionation, the key liquidus phases controlling the composition of melts (Storey, 1995). Low values of Sr/Y (0.9-5.2), La/Yb (< 14) and $(Gd/Lu)_N$ = 0.64-2.19 point to plagioclase as a stable residual phase and suggest crystallization of mineral phases in the plagioclase stability field (e.g., Wang et al., 2012; Fig. 10). Considering the above, it is possible to hypothesize that the origin of studied rocks included subduction-related, mantle derived, melts and crust-derived magmas in the area in which a melting-assimilation-storage homogenization (MASH) process occurs. Hydrothermal post-depositional alteration parageneses of studied tuffs are essentially devoid of ferromagnesian phases (Table 2) thus further corroborating the role of the acidic crust in the formation of tuffs' parental magmas.

A continuous increase of the contribution of the continental crust and consequent enrichment by the crustal component is well documented despite a relatively short deposition of pyroclastic material within the Northwestern Croatian Triassic Rift Basin (~ 3 Ma; late Anisian-early Ladinian - Kukoč et al., in review). This is clearly suggested by a steady decrease in the initial $\varepsilon_{Nd}$ values coupled with an increase in the content of Pb during the deposition time of pyroclastic material (Figs. 3, 7a1, 8; Tables 3 and 4). The above indicates a significant increase in magma saturation with the continental crust in a short period of only ~ 3

Table 4 - Nd isotope data for rhyolitic tuffs from the Kuna Gora, Strahinjščica and Ivanščica Mts.

| Sample | Lithotype | Sm/Nd | $^{147}Sm/^{144}Nd$ | $^{143}Nd/^{144}Nd$ | $^{143}Nd/^{144}Nd_{(t)}$ | $\varepsilon_{Nd(t)}$[a] | Time (t)[b] |
|---|---|---|---|---|---|---|---|
| GK I-19 | VC | 0.18218 | 0.110136 | 0.512342 ($5*10^{-6}$) | 0.512166 | -3.08 | 244 Ma |
| GK II-2.80 | VC | 0.22590 | 0.136566 | 0.512344 ($8*10^{-6}$) | 0.512126 | -3.86 | 244 Ma |
| BR II-15.45 | VCC | 0.19863 | 0.136565 | 0.512340 ($5*10^{-6}$) | 0.512122 | -3.94 | 244 Ma |
| BR II-23.20 | VCC | 0.19533 | 0.118086 | 0.512292 ($6*10^{-6}$) | 0.512103 | -4.30 | 244 Ma |
| SEK-6.75 | VC | 0.20826 | 0.125903 | 0.512386 ($7*10^{-6}$) | 0.512185 | -2.71 | 244 Ma |
| SEK-37.35 | VC | 0.22570 | 0.136443 | 0.512288 ($6*10^{-6}$) | 0.512070 | -4.95 | 244 Ma |

Errors in brackets for Nd isotopic ratios are given at the 2σ-level. The method of calculating the errors is presented in the analytical techniques chapter. $^{147}Sm/^{144}Nd$ calculated from the ICP-MS concentrations of Sm and Nd following equation: $^{147}Sm/^{144}Nd = (Sm/Nd)*[0.53151+0.14252*^{143}Nd/^{144}Nd]$. [a] Initial $\varepsilon_{Nd(t)}$ calculated assuming $I^{o}_{CHUR}$ = 0.512638, $(^{147}Sm/^{144}Nd)^{o}_{CHUR}$ = 0.1966, and $\lambda_{Sm} = 6.54*10^{-12}$ $y^{-1}$. [b]Corresponding time for the initial $\varepsilon_{Nd}$ and initial isotopic ratios for Nd. VC = vitroclastic tuff; VCC = vitrocrystalloclastic tuff.

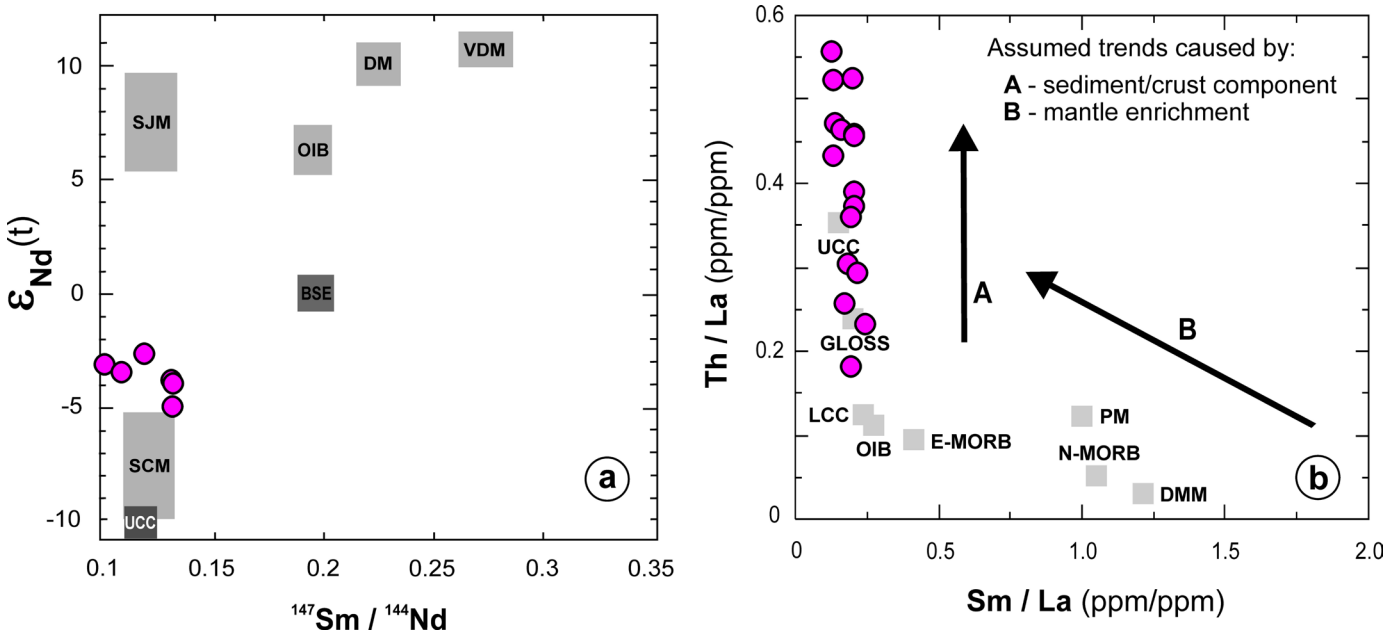


Fig. 8 - a) $^{147}Sm/^{144}Nd$ - $\varepsilon_{Nd(t)}$ isotope ratios diagram [Hypothetical mantle sources: DM = depleted mantle (not refractory), OIB = ocean island basalts, VDM = very depleted mantle (refractory), SJM = subducted juvenile material (subducted oceanic crust; slab with little pelagic sediment), SCM = subducted continental material, BSE = bulk silicate earth and UCC = upper continental crust (Chauvel et al., 2014). The observed compositions and hypothetical end members sources calculated for the Middle Triassic following Swinden et al. (1990)]; b) Th/La - Sm/La diagram (after Plank, 2005) for the acidic pyroclastic rocks from the Kuna Gora, Strahinjščica and Ivanščica Mts. Abbreviations: [N-MORB = normal mid-ocean ridge basalts; E-MORB = enriched MORB; OIB = ocean island basalts; PM = primitive mantle (Sun and McDonough, 1989)]; [UCC = upper continental crust; LCC = lower continental crust (Rudnick and Gao, 2014)]; GLOSS = global subduction sediment (Plank and Langmior, 1998); DMM = depleted MORB mantle (Workman and Hart, 2005).

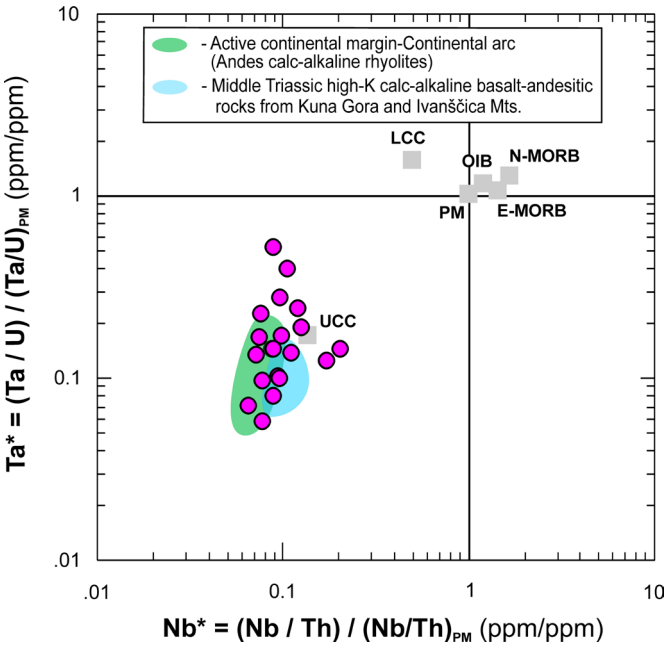


Fig. 9 - Discrimination diagram for the acidic pyroclastic rocks from the Kuna Gora, Strahinjščica and Ivanščica Mts. $(Nb/Th)/(Nb/Th)_{PM}$ - $(Ta/U)/(Ta/U)_{PM}$ (after Niu and Batiza, 1997; Niu et al., 1999). Abbreviations: [N-MORB = normal mid-ocean ridge basalts; E-MORB = normal mid-ocean ridge basalts; OIB = ocean island basalts; PM = primitive mantle (Sun and McDonough, 1989)]; [UCC = upper continental crust; LCC = lower continental crust (Rudnick and Gao, 2014)]. Data for Andes calc-alkaline rhyolites (Riley et al., 2001; Garrison et al., 2011) and Middle Triassic high-K calc-alkaline basalt-andesitic rocks from Kuna Gora and Ivanščica Mts. (Slovenec et al., 2020; Slovenec and Šegvić, 2021) are plotted for correlation constrains.

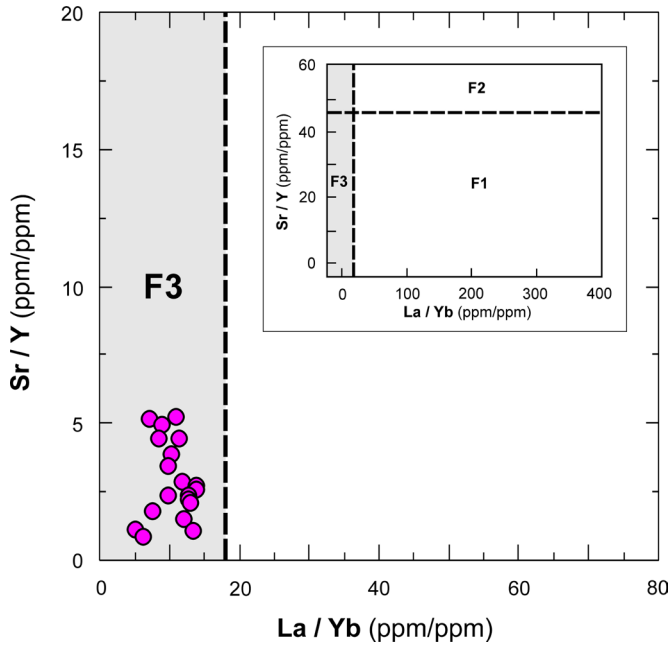


Fig. 10 - Discrimination diagram for the acidic pyroclastic rocks from the Kuna Gora, Strahinjščica and Ivanščica Mts. La/Yb - Sr/Y diagram (Halder et al., 2021 and referencs therein). Abbreviations: F1 = garnet stabillity field, little/no plagioclase, F2 = garnet and plagioclase stabillity field, F3 = plagioclase stabillity field, little/no garnet.

Ma during late Anisian-early Ladinian. The changes in the initial $\varepsilon_{Nd}$ is indicative of the variations in the crust/melt ratio during an inconsistent magma flow through the crust as inferred by Strock et al. (2020) for similar volcano-sedimentary successions in the Italian Southern Alps. Based on the presented discussion, it is reasonable to infer that during a relatively short magmatic cycle characteristic for northwestern Tethys during the late Anisian to early Ladinian, the flow of mantle-derived magmas progressively abated while its interaction with the neighboring acidic crust had intensified.

**Tectonomagmatic and geodynamic significance**

Pyroclastic rocks of the study area feature a significant enrichment in LREE coupled with a selective depletion in HFSE as well as prominent negative anomalies of the Nb-Ta pair and Ti. These characteristics support a strong subduction influence (Pearce, 1982; Arculus and Powel, 1986; Hawkesworth et al., 1993; Fig. 7a1, b1). The primitive mantle normalized multielement diagram distribution patterns (Fig. 7b1), as well as the ratios of selected trace elements (Fig. 11a to d) are seemingly analogous to extrusive/pyroclastic rocks formed in an Andean-type conti-

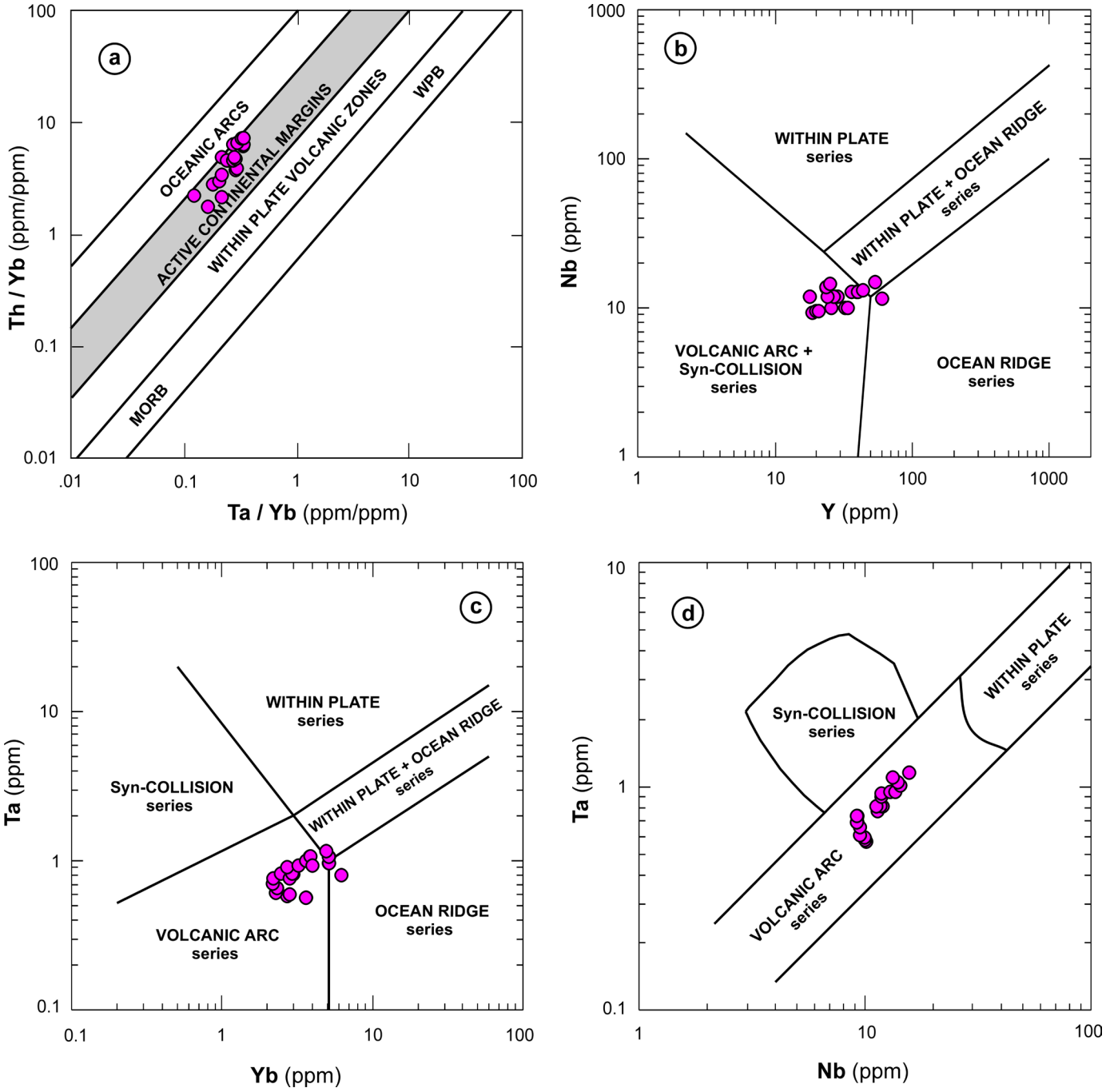


Fig. 11 - Discrimination diagrams for the acidic pyroclastic rocks from the Kuna Gora, Strahinjščica and Ivanščica Mts. **(a)** Ta/Yb - Th/Yb diagram (Gorton and Shandl, 2000). **(b)** Y - Nb diagram (Pearce et al., 1984). **(c)** Yb - Ta diagram (Pearce et al., 1984). **(d)** Nb - Ta diagram (Harris et al., 1986).

nental margin volcanic arc environment (e.g., Riley et al., 2001; Garrison et al., 2011). The chemical composition of the tuffs studied herein is however largely inherited from older arc-related lithologies related to subduction of the Paleotethys, which were affected by partial melting (Slovenec and Šegvić, 2021). Therefore, the presented chemistry that indicates the existence of a volcanic arc does not necessarily reflect the actual tectonomagmatic environment of the formation of the studied tuffs. Their origin can be explained using the concepts of i) Stampfli and Borel (2002; 2004) and Stampfli and Hochard (2009) who favour a possible active Middle Triassic northward subduction of the Hercynian Paleotethyan lithosphere beneath the Eurasian Plate coupled with a mantle wedge wet melting (Fig 12a), or that of ii) Van Hinsberger et al. (2020) and Van Hinsberger and Schouten (2021) who linked the opening of the Neotethys to an southwestward subduction of Paleotethyan lithosphere below the northeastern Greater Adria margin which was followed by the roll-back of the Paleotethys slab (Fig. 12b). In light with the latter concept which excludes an active subduction in lieu of a passive continental rifting along mid-Triassic margins of Greater Adria, the formation and deposition of studied tuffs within the Northwestern Croatian Triassic Rift Basin results from i) partial melting of the heterogeneous lithospheric (subcontinental) mantle, which had been metasomatized during an earlier Hercynian subduction event(s) in the Late Paleozoic (Saccani et al., 2015) and ii) subordinated to the processes related to the melting of the upper continental crust and fractionation as suggested by Slovenec and Šegvić (2021) for the coeval basalts/andesites of this area. Repetitive volcanic eruptions made use of tectonically weakened zones of the crust to facilitate the ascent of acidic magma(s) to the surface eventually producing rhyolitic tephra. Pyroclastic material was further transported via density flows and surges or as the air-born material and finally deposited in an intracontinental simple or half-graben syn-rift basin (e.g., the Northwestern Croatian Triassic Rift Basin; Kukoč et al., in review; Figs. 3 and 12) alongside with a deep-sea siliciclastic and carbonate sediment.

## CONCLUSIONS

- The Middle Triassic (late Anisian-early Ladinian) acidic pyroclastic rocks intercalated by deep-sea siliciclastic and carbonate sediments make an integral part of the volcanic-sedimentary succession of the Northwestern Croatian Triassic Rift Basin which stands as the southernmost segment of the geotectonic unit of the Southern Alps.
- Three lithotypes of the *Pietra Verde* tuffs are determined: vitroclastic, vitrocrystalloclastic, and crystalloclastic. The deposits were largely formed through the pyroclastic density currents and air-fall transport. The tuffs' appearance and variability suggest formation through numerous explosive volcanic eruptions.
- Studied rhyolitic tuffs are subalkaline middle to high-K calc-alkaline, and shoshonitic. The geochemical data support a subduction influence, while negative values of initial εNd and high Pb content are indicative of a significant impact of the continental material/crust.
- The origin of studied tuffs includes the contamination of a subduction-generated magma by lithospheric mantle melts and an enrichment of the sources by subduction related crustal melts. In addition to partial melting of the heterogeneous lithospheric (subcontinental) mantle, subordinated melting of the continental crust, the genesis of studied rocks have included fractional crystallization.
- As per the suggested geodynamic model, the formation of studied tuffs could have occurred in the continental margin volcanic arc(?) environment which came to being during an active(?) northward subduction of the Paleotethyan lithosphere beneath the Eurasian Plate or, alternatively, more likely, during the passive continental rifting along the margins of the Greater Adria Plate.

## ACKNOWLEDGEMENTS

This work has been supported by the Croatian Science Foundation under the project (IP-2019-04-3824). Critical comments and constructive reviews by three anonymous reviewers, as well as the editorial handling by Yildrim Dilek, contributed significantly to the manuscript quality.

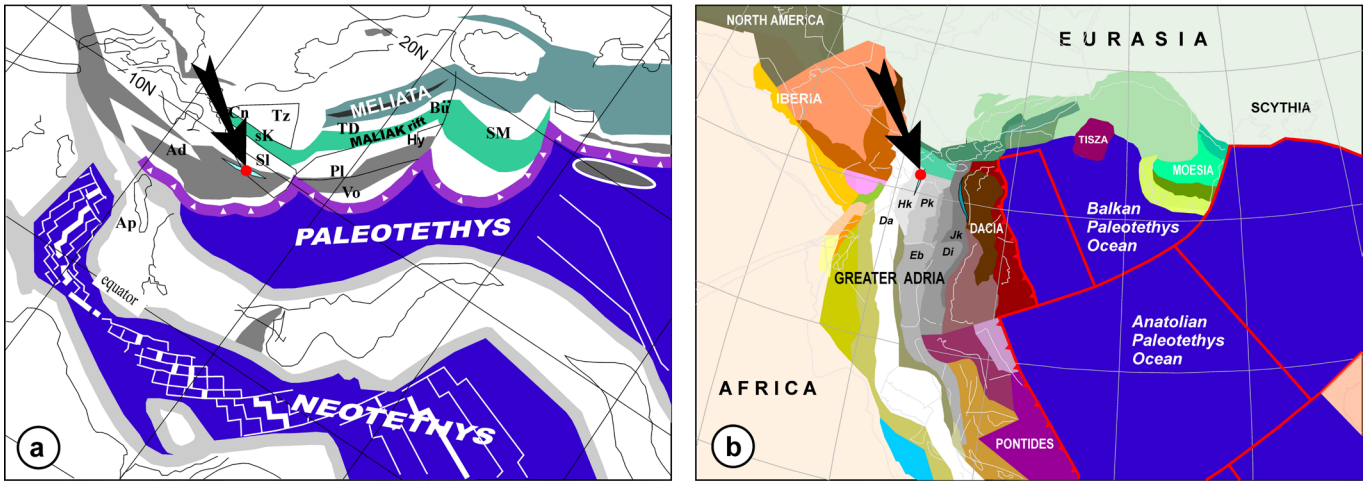


Fig. 12 - The Anisian-Ladinian (~ 240 Ma) palaeogeographic reconstruction of the Mediterranean region: a) simplified and modified after Stampfli and Borel (2004) and Alparslan and Dilek (2018) [Ad = Adria Plate *s. str.*, Ap = Apulia *s. str.*, Bü = Bükk, Cn = Carnic-Julian, Hy = Hydra, Pl = Pelagonian, sK = south-Karawanken fore arc, Sl = Slavonia, SM = Serbo-Macedonian, TD = Trans-Danubian, Tz = Tisza, Vo = Vourinos (Pindos)] and, b) simplified and slightly modified after Van Hinsbergen et al. (2020) [Da = Dalmatian Nappe, Di = Drina-Ivanjica Nappe, Eb = East Bosnian-Durmitor Nappe, Jk = Jadar-Kopaonik Nappe, Hk = High-Karst Nappe, Pk = Pre-Karst Nappe] with location of the Northwestern Croatian Triassic Rift Basin and investigation area of Kuna Gora, Strahinjščica and Ivanščica Mts (marked with black arrow and red dot symbol). The reader is referred to the PDF version of the article for a colour version.

## REFERENCES


Alparslan G. and Dilek Y., 2018. Seafloor spreading structure, geochronology, and tectonic evolution of the Küre ophiolite, Turkey: a Jurassic continental backarc basin oceanic lithosphere in southern Eurasia. Lithosphere, 10: 14-34.

Arbiol C., Layne G.D., Zanoni G. and Šegvić B., 2021. Characteristics and genesis of phyllosilicate hydrothermal assemblages from Neoproterozoic epithermal Au-Ag mineralization of the Avalon Zone of Newfoundland, Canada. Appl. Clay Sci., 202. https://doi.org/10.1016/j.clay.2020.105960

Armstrong J.T., 1991. Quantitative elemental analysis of individual microparticles with electron beam instruments. In: Heinrich, K.F.J., Newbury, D.E. (eds) Electron Probe Quantitation. Springer, Boston, MA. https://doi.org/10.1007/978-1-4899-2617-3_15, pp.261-315.

Bonadiman C., Coltorti M. and Siena F., 1994. Petrogenesis and T-$fO_2$ estimates of Mt. Monzoni complex (Central Dolomites, Southern Alps): a Triassic shoshonotic intrusion in a transcurrent geodynamic setting. Eur. J. Miner., 6: 943-966.

Casetta F., Coltorti M. and Marrocchino E., 2018. Petrological evolution of the middle Triassic Predazzo intrusive complex, Italian Alps. Intern. Geol. Rev., 60: 977-997.

Castellarin A., Lucchini F., Rossi P.L., Selli L. and Simboli G., 1988. The Middle Triassic magmatic-tectonic arc developed in the Southern Alps. Tectonophysics, 146: 79-89.

Chauvel C., Garçon M., Bureau S., Besnault A., Jahn B-M., et al. 2014. Constraints from loess on the Hf-Nd isotopic composition of the upper continental crust. Earth Planet. Sci. Lett., 38: 48-58.

Cook E., 1965. Stratigraphy of Tertiary volcanic rocks in eastern Nevada. Nevada Bureau of Mines and Geology open-file report, 11: 1-66.

Cuadros J., Caballero E., Huertas F.J., Jiménez de Cisneros C., Huertas F. and Linares J., 1999. Experimental alteration of volcanic tuff: smectite formation and effect on 18O isotope composition. Clays Clay Miner., 47: 769-776.

Dana J.D., Klein C. and Hurlbut C.S., 1993. Manual of mineralogy, Wiley, New York, 681 pp.

Deer W.A., Howie R.A. and Zussman J., 1992. An introduction to the rock-forming minerals, 3rd Ed. Longman Group Limited, London, 489 pp.

De Min A., Velicogna M., Ziberna L., Chiaradia M., Alberti A. and Marzoli A., 2020. Triassic magmatism in the European Southern Alps as an early phase of Pangea break-up. Geol. Mag., 157: 1800-1822.

Donoghue E., Troll V.R., Harris C., O'Halloran A., Walter T.R. and Pérez Torrado F.J., 2008. Low-temperature hydrothermal alteration of intra-caldera tuffs, Miocene Tejeda caldera, Gran Canaria, Canary Islands. J. Volcan. Geotherm. Res., 176: 551-564.

Du Riche Preller C.S., 1916. The "Pietre Verdi" of the Piémontese Alps. Geol. Mag., 3: 156-163.

Eby G.N., 1990. The A-type granites: A review of their occurrence and chemical characteristics and speculations on their petrogenesis. Lithos, 26: 115-134.

Ertek N. and Öner F., 2008. Mineralogy, geochemistry of altered tuff from Cappadocia (Central Anatolia) and its use as potential raw material for the manufacturing of white cement. Appl. Clay Sci., 42: 300-309.

Garrison J.M., Davidson J.P., Minard Hall M. and Mothes P., 2011. Geochemistry and petrology of the most recent deposits from Cotopaxi Volcano, NorthernVolcanic Zone, Ecuador. J. Petrol., 52: 1641-1678.

Goričan Š., Halamić J., Grgasović T. and Kolar-Jurkovšek T., 2005. Stratigraphic evolution of Triassic arc-backarc system in northwestern Croatia. Bull. Soc. Géol. Fr., 176: 3-22.

Gorton M.P. and Shandl E.S., 2000. From continents to island arcs: A geochemical index of tectonic setting for arc-related and within-plate felsic to intermediate volcanic rocks. Can. Miner., 38: 1065-1073.

Haas J. and Kovács S., 2001. The Dinaridic-Alpine connection - as seen from Hungary. Acta Geol. Hung., 44: 345-362.

Halder M., Paul M. and Sensarma S., 2021. Rhyolites in continental mafic large igneous provinces: Petrology, geochemistry and petrogenesis. Geosci. Front., 12: 53-80.

Harangi Sz., Szabó Cs., Józsa S., Szoldán Zs., Árva-Sós E., Balla M. and Kubovics I., 1996. Mesozoic igneous suites in Hungary: Implications for genesis and tectonic setting in the northwestern part of Tethys. Intern. Geol. Rev., 38: 336-360.

Harris N.B.W., Pearce J.A. and Tindle A.G., 1986. Geochemical characteristics of Collision-Zone magmatism. In: M.P. Coward and A.C. Ries (Eds.), Collision tectonics. Geol. Soc. London Spec. Publ. 19: 67-81.

Hawkesworth C.J., Gallagher K., Hergt J.M. and Mcdermott F., 1993. Trace element fractionation processes in the generation of island arc basalts. In: K.G. Cox, D.P. Mckenzie and R.S. White (Eds.), Melting and melt movement in the Earth. Philos. Trans. Royal Soc. London, A342: 179-191.

Jochum K.P., Willbold M., Raczek I., Stoll B. and Herwig K., 2005. Chemical characterisation of the USGS Reference Glasses GSA-1G, GSC-1G, GSD-1G, GSE-1G, BCR-2G, BHVO-2G and BIR-1G Using EPMA, ID-TIMS, ID-ICP-MS and LA-ICP-MS. Geostand. Geoanalyt. Res., 29: 285-302.

Kretz R., 1983. Symbols for rock-forming minerals. Am. Miner., 68: 277-279.

Kukoč D., Smirčić D., Grgasović T., Horvat M., Belak M., Japundžić D., Kolar-Jurkovšek T. Šegvić B., Badurina L., Vukovski M. and Slovenec Da., in review. Biostratigraphy and facies description of Middle Triassic rift related volcano-sedimentary successions on the junction of the Southern Alps and the Dinarides (NW Croatia). Intern. J. Earth Sci.

Lustrino M., Abbas H., Agostini S., Gaggiati M., Carminati E. and Gianolla P., 2019. Origin of Triassic magmatism of the Southern Alps (Italy): constraints from geochemistry and Sr-Nd-Pb isotopic ratios. Gondw. Res., 75: 218-238.

Marci V., Šćavničar S. and Sijarić G., 1982. Petrogenesis of the volcanic rocks of Ivanščica Mt. (River Željeznica). 10th Cong. Geol. Jugosl., Budva. Zbornik radova, 1: 329-335 (in Croatian, with English summary).

Marci V., Ščavnićar S. and Sijarić G., 1984. The new data about volcanic rocks of Ivanščica mountain. Geol. Vjesnik, 37: 97-104 (in Croatian, with English abstract).

Neubauer F., Liu Y., Cao S. and Yuan S., 2019. What is the Austroalpine mega-unit and what are the potential relations to Paleotethys Ocean remnants of southeastern Europe? Geol. Carpath., 70: 16-20.

Niu Y. and Batiza R., 1997. Trace element evidence from seamounts for recycled oceanic crust in the eastern Pacific mantle. Earth Planet. Sci. Lett., 148: 471-483.

Niu Y., Collerson K.D., Batiza R., Wendt J.I. and Regelous M., 1999. The origin of E-Type MORB at ridges far from mantle plumes: the East Pacific Rise at 11°20'. J. Geophys. Res., 104: 7067-7087.

Pamić J., 1984. Triassic magmatism of the Dinarides in Yugoslavia. Tectonophysics, 109: 273-307.

Pamić J. and Balen D., 2005. Interaction between permo-Triassic rifting, magmatism and initiation of the Adriatic-Dinaridic carbonate platform (ADCP). Acta Geol. Hungar., 48: 181-204.

Pamić J. and Tomljenović B., 1998. Basic geological data on the Croatian part of the Mid-Transdanubian Zone as exemplified by Mt. Medvednica located along the Zagreb-Zemplen Fault Zone. Acta Geol. Hungar., 41: 389-400.

Pearce J.A., 1982. Trace element characteristics of lavas from destructive plate boundaries. In: R.S. Thorpe (Ed.), Andesites. Wiley, New York, p. 525-548.

Pearce J.A. and Norry M.J., 1979. Petrogenetic Implications of Ti, Zr, Y, and Nb variations in volcanic rocks. Contrib. Miner. Petrol., 69: 33-47.

Pearce J.A., Harris N. and Tindle A.G., 1984. Trace element discrimination diagrams for the tectonic interpretation of granitic rocks. J. Petrol., 25: 956-983.

Peccerillo R. and Taylor S.R., 1976. Geochemistry of Eocene calc-alkaline volcanic rocks. Earth Planet. Sci. Lett., 36: 121-132.

Plank T., 2005. Constraints from Th/La on sediment recycling at subduction zones and evolution of the continents. J. Petrol., 46: 921-994.

Plank T. and Langmiur C.H., 1998. The chemical composition of subducting sediment and its consequences for the crust and mantle. Chem. Geol., 145: 325-394.

Riley T.R., Leat P.T., Pankhrust R.J. and Harris C., 2001. Origins of large volume rhyiolitic volcanism in the Antartic peninsula and Patagonia by the crustal melting. J. Petrol., 42: 1043-1065.

Rollinson H.R., 1993. Using geochemical data: evaluation, presentation, interpretation. Longman, 352 pp.

Rudnick R.L. and Gao S., 2014. Composition of the continental crust. In: H.D. Holland and K.K. Turekian (Eds.), Treatise on Geochemistry, 2nd Ed. Elsevier Inc., p. 1-51.

Saccani E., Dilek Y., Marroni M. and Pandolfi L., 2015. Continental margin ophiolites of Neotethys: remnants of ancient Ocean-Continent Transition Zone (OCTZ) lithosphere and their geochemistry, mantle sources and melt evolution patterns. Episodes, 38: 230-249.

Schmid R., 1981. Descriptive nomenclature and classifcation of pyroclastic deposits and fragments: recommendations of the IUGS Subcommission on the Systematics of Igneous Rocks. Geology, 9: 41-43.

Schmid S.M., Bernoulli D., Fügenschuh B., Matenco L., Scheffer S., Schuster R., Tischler M. and Ustaszewski K., 2008. The Alpine-Carpathian-Dinaridic orogenic system: correlation and evolution of tectonic units. Swiss J. Geosci., 101: 139-183.

Šebečić B., 1969. Sedimentary rocks of Strahinjščica Mountain. Geol. Vjesnik, 23: 241-256 (in Croatian, with English abstract).

Šegvić B., Lukács R., Mandic O., Strauss P., Badurina L., Guillong M. and Harzhauser M., 2022. U-Pb zircon age and mineralogy of St. Georgen halloysite tuff shed light on the timing of the middle Badenian (mid-Langhian) transgression, ash dispersal, and paleoenvironmental conditions in the southern Vienna Basin, Austria. J, Geol. Soc. London. jgs2022-106. https://doi.org/10.1144/jgs2022-106

Šimunić An. avd Šimunić Al., 1997. Triassic deposits of Hrvatsko Zagorje. Geol. Croat., 50: 243-250.

Šimunić An., Pikija M. and Hećimović I., 1982. Osnovna geološka karta SFRJ 1:100000, list Varaždin L33-69 [Basic Geological Map of SFRY 1:100000. Varaždin sheet - in Croatian]. Inst. Geol, Istraživanja Zagreb, Savezni Geol. Zavod Beograd.

Slovenec D. and Šegvić B., 2021. Middle Triassic high-K calc-alkaline effusive and pyroclastic rocks from the Zagorje-Mid-Transdanubian Zone (Mt. Kuna Gora; NW Croatia): mineralogy, petrology, geochemistry and tectono-magmatic affinity. Geol. Acta, 19: 1-23.

Slovenec Da., Šegvić B., Halamić J., Goričan Š. and Zanoni G., 2020. An ensialic volcanic arc along the northwestern edge of Palaeotethys-Insights from the Mid-Triassic volcanosedimentary succession of Ivanščica Mt. (northwestern Croatia). Geol. J., 55: 4324-4351.

Smirčić D., Kolar-Jurkovšek T., Aljinović D., Barudžija U., Jurkovšek B.and Hrvatović H., 2018. Stratigraphic definition and correlation of the Middle Triassic volcaniclastic facies in the External Dinarides: Croatia and Bosnia and Herzegovina. J. Earth Sci., 29: 864-878.

Stampfli G.M. and Borel G.D., 2002. A plate tectonic model for the Paleozoic and Mesozoic constrained by dinamic plate boundaries and restored synthetic ocean isochrons. Earth Planet. Sci. Lett., 196: 17-33.

Stampfli G.M. and Borel G.D., 2004. The TRANSMED transects in space and time: Constraints on the paleotectonic evolution of the Mediterranean domain In: W. Cavazza, F. Roure, W. Spakman, G.M. Stampfli and P.A. Ziegler (Eds.), The TRANSMED Atlas: the Mediterranean Region from crust to mantle. Springer-Verlag, Berlin, p. 53-80.

Stampfli G.M. and Hochard C., 2009. Plate tectonics of the Alpine realm. Geol. Soc. London Spec.l Publ., 327: 89-111.

Stampfli C., Hochard C., Vérard C., Wilhem J. and Von Raumer J.F., 2013. The formation of Pangea. Tectonophysics, 593: 1-19.

Storck J.C., Brack P., Wotzlaw J.F. and Ulmer P., 2018. Timing and evolution of Middle Triassic magmatism in the Southern Alps (Northern Italy). J. Geol. Soc. London, 176: 253-268.

Storck J.C., Wotzlaw J.F., Karakas Ö., Brack P., Gerdes A. and Ulmer P., 2020. Hafnium isotopic record of mantle-crust interaction in an evolving continental magmatic system. Earth Planet. Sci. Lett., 535: 116100. https://doi.org/10.1016/j.epsl.2020.116100.

Storey B.C., 1995. The role of mantle plumes in the continental break up: case histories from Gondwanaland. Nature, 377: 301-308.

Sun S.S. and Mcdonough W.F., 1989. Chemical and isotopic systematics of oceanic basalts: implications for mantle composition and processes. In: A.D.Saunders and M.J. Norry (Eds.), Magmatism in ocean basins. Geol. Soc. London Spec. Publ., 42: 313-345.

Swinden H.S., Jenner G.A., Fryer B.J., Hertogen J. and Roddick J.C., 1990. Petrogenesis and paleotectonic history of the Wild Bight Group, an Ordovician rifted island arc in central Newfoundland. Contrib. Miner. Petrol., 105: 219-241.

Tanaka T., Togashi S., Kamioka H., Amakawa H., Kagami H., Hamamoto T., et al. 2000. JNdi-1: A neodymium isotopic reference in consistency with Lajolla neodymium, Chem. Geol., 168: 279-281.

Taylor S.R. and McLennan S.M., 1985. The continental crust: its composition and evolution. Blackwell Sci. Publ., Oxford, 312 pp.

Tian W., Campbell I.H., Allen C.M., Guan P., Pan W., Chen M., Yu H. and Zhu W., 2010. The Tarim picrite-basalt-rhyolite suite, a Permian flood basalt from Northwest China with contrasting rhyolites produced by fractional crystallization and anatexis. Contrib. Miner. Petrol., 160: 407-425.

Tomljenović B., Csontos L., Emo Márton E. and Márton P., 2008. Tectonic evolution of the northwestern Internal Dinarides as constrained by structures and rotation of Medvednica Mountains, North Croatia. Geol. Soc. London Spec. Publ., 298: 145-167.

Trubelja F., Burgath K.P. and Marchig V., 2004. Triassic magmatism in the area of the Central Dinarides (Bosnia and Herzegovina): Geochemical resolving of tectonic setting. Geol. Croat., 57: 159-170.

Van der Hinsbergen J.J. and Schouten T.L.A., 2021. Deciphering paleogeography from orogenic architecture: constructing orogens in a future supercontinent as thought experiment. Am. J. Sci., 321: 955-1031.

Van der Hinsbergen J.J., Torsvik T.H., Schmid S.M., Matenco L.C., Maffione M., Vissers R.L.M., Gürer D. and Spakman W., 2020. Orogenic architecture of the Mediterranean region and kinematic reconstruction of its tectonic evolution since the Triassic. Gondw. Res., 81: 79-229.

Van Gelder I.E., Matenco L., Willingshofer E., Tomljenović B., Andriessen P.A.M., Ducea M.N., Beniest A. and Gruić A., 2015. The tectonic evolution of a critical segment of the Dinarides-Alps connection: Kinematic and geochronological inferences from the Medvednica Mountains, NE Croatia. AGU Tectonics, 10. 1002/2015TC003937.

Vlahović I., Tišljar J., Velić I. and Matičec D., 2005. Evolution of the Adriatic Carbonate Platform: Paleogeography, main events and depositional dynamics. Palaeo., Palaeo., Palaeo., 220: 333-360.

Wang Q., Chung S.L., Li X.H., Wyman D., Li Z.X., Sun W.D., Qiu H.N., Liu Y.S. and Zhu Y.T., 2012. Crustal melting and flow beneath northern Tibet: evidence from Mid-Miocene to Quaternary strongly peraluminous rhyolites in the Southern Kunlun Range. J. Petrol., 53: 2523-2566.

Weis D., Kieffer B., Maerschalk C., Barling J., de Jong J., Willians G.A., Hanano D., Pretorius W., Scoates J.S., Goolaerts A., Friedman R.M. and Mahoney J.B., 2006. High-precision isotopic characterization of USGS reference materials by TIMS and MC-ICP-MS. Geochem., Geophys., Geosyst., 7: 1-30.

Wilson M., Downes H. and Cebria J.M., 1995. Contrasting fractionation trends in coexisting continental alkaline magma series: Cantal, Massif Central, France. J. Petrol., 36: 1729-1753.

Winchester J.A. and Floyd P.A., 1977. Geochemical discrimination of different magma series and their differentiation products using immobile elements. Chem. Geol., 20: 325-343.

Workman R.K. and Hart S.R., 2005. Major and trace element composition of the depleted MORB mantle (DMM). Earth Planet. Sci. Lett., 231: 53-72.

Zulauf G., Dörr W., Marko L. and Krahl J., 2018. The late Eo-Cimmerian evolution of the external Hellenides: constraints from microfabrics and U-Pb detrital zircon ages of Upper Triassic (meta)sediments (Crete, Greece). Intern. J. Earth Sci., 107: 2859-2894.

Received, September 29, 2022
Accepted, December 12, 2022